Magnetic structures of $R_5Ni_2In_4$ and $R_{11}Ni_4In_9$ (R = Tb and Ho): strong hierarchy in the temperature dependence of the magnetic ordering in the multiple rare-earth sublattices

2015 J. Phys.: Condens. Matter 27 476001

(http://iopscience.iop.org/0953-8984/27/47/476001)

IOP Publishing

Journal of Physics: Condensed Matter

J. Phys.: Condens. Matter **27** (2015) 476001 (20pp)

doi:10.1088/0953-8984/27/47/476001

Magnetic structures of $R_5Ni_2In_4$ and $R_{11}Ni_4In_9$ (R = Tb and Ho): strong hierarchy in the temperature dependence of the magnetic ordering in the multiple rare-earth sublattices

C Ritter[1], **A Provino**[2,3,4], **P Manfrinetti**[2,3,4], **V K Pecharsky**[2,5], **K A Gschneidner Jr**[2,5] **and S K Dhar**[6]

[1] Institut Laue-Langevin, BP 156, 38042 Grenoble, France
[2] The Ames Laboratory, U.S. Department of Energy, Iowa State University, Ames, IA 50011–3020, USA
[3] Department of Chemistry, University of Genova, Via Dodecaneso 31, 16146 Genova, Italy
[4] Institute SPIN-CNR, Corso Perrone 24, 16152 Genova, Italy
[5] Department of Materials Science and Engineering, Iowa State University, Ames, IA 50011–2300, USA
[6] Department of Condensed Matter Physics & Material Science, T.I.F.R., Homi Bhabha Road, Mumbai 400005, India

E-mail: ritter@ill.fr

Received 4 August 2015, revised 14 September 2015
Accepted for publication 9 October 2015
Published 9 November 2015

Abstract

The magnetic properties and magnetic structures of the $R_5Ni_2In_4$ and the microfibrous $R_{11}Ni_4In_9$ compounds with R = Tb and Ho have been examined using magnetization, heat capacity, and neutron diffraction data. Rare earth atoms occupy three and five symmetrically inequivalent rare earth sites in $R_5Ni_2In_4$ and $R_{11}Ni_4In_9$ compounds, respectively. As a result of the intra- and inter-magnetic sublattice interactions, the magnetic exchange interactions are different for various rare earth sites; this leads to a cascade of magnetic transitions with a strong hierarchy in the temperature dependence of the magnetic orderings.

A transition at $T_C = 125$ K in $Tb_5Ni_2In_4$ [$\kappa_1 = (0, 0, 0)$] leads to a ferro/ferrimagnetic order where the magnetic ordering in one of the three R-sublattices leads to the ordering of another one; the third sublattice stays non-magnetic. New magnetic Bragg peaks appearing below $T_N = 20$ K can be indexed with the incommensurate magnetic propagation vector $\kappa_2 = (0, 0.636, ½)$; at $T_N = 20$ K a cycloidal spin order, which acts mostly upon the third R-sublattice, occurs. $Ho_5Ni_2In_4$ establishes first antiferromagnetism [$\kappa = (0, 0, 0)$] at $T_N = 31$ K on two R-sublattices; then the system becomes ferro/ferrimagnetic at $T_C = 25$ K with the third sublattice ordering as well. $Tb_{11}Ni_4In_9$ has three magnetic transitions at $T_C = 135$ K, $T_{N1} = 35$ K and at $T_{N2} = 20$ K; they are respectively coupled to the appearance of different propagation vectors [$\kappa_1 = (0, 0, 0)$, $\kappa_2 = (0, 0, ½)$, $\kappa_3 = (0, 1, ½)$], which themselves are operating differently on the five different R-sublattices. Two sublattices remain mostly ferromagnetic down to lowest temperature while the three others are predominantly coupled antiferromagnetically. In $Ho_{11}Ni_4In_9$ a purely antiferromagnetic order, described by four different magnetic propagation vectors [$\kappa_1 = (0, 0.62, 0)$, $\kappa_2 = (0, 1, 0)$, $\kappa_3 = (0, 0, ½)$, $\kappa_4 = (0, 1, ½)$], succeedingly includes all five different sublattices on cooling through transitions at $T_{N1} = 22$ K, $T_{N2} = 12$ K, $T_{N3} = 8$ K and $T_{N4} = 7$ K. The strength of the magnetic interactions of the different sublattices can be linked to structural details for both $R_5Ni_2In_4$ and $R_{11}Ni_4In_9$ compounds.

Keywords: rare earths nickel indides, rare earth intermetallics, neutron diffraction, magnetic structures

(Some figures may appear in colour only in the online journal)

1. Introduction

Two families of compounds with close stoichiometries, namely $R_{11}Ni_4In_9$ and $R_5Ni_2In_4$, are known to exist in the R-Ni-In (R = rare earth) systems. The stoichiometry of both families can be described by the general formula $R_{m+n}M_{2n}X_m$ (M = transition metal, X = In or B). The $R_{11}Ni_4In_9$ intermetallics ($m = 9$, $n = 2$) crystallize with the $Nd_{11}Pd_4In_9$ structure type (*oC*48, *Cmmm, Z* = 2) [1]. This structure is formed from n fragments of RNi$_2$ (AlB_2-type) and m fragments of RIn (CsCl-type). Here, layers of R atoms alternate with layers of Ni/In atoms along the short c axis of the orthorhombic unit cell. The formation of the $R_{11}Ni_4In_9$ phase was originally reported for R = La-Nd, Sm, Gd, Tb, and Y [2]. More recently, we found that the $R_{11}Ni_4In_9$ phase forms for all of the trivalent heavy lanthanides, including R = Dy, Ho, Er, Tm and Lu. The compound does not exist for R = Sc nor for the divalent Eu and Yb [3–5]. Further, we also demonstrated the formation of the isostructural $R_{11}Pd_4In_9$ and $R_{11}Pt_4In_9$ phases. All $R_{11}M_4In_9$ compounds (M = Ni, Pd, Pt) exhibit an unusual and interesting fibrous morphology: these compounds solidify from the melt as bundles of nano/microfibers [4–6].

Measurements of physical properties on oriented microfibrous specimens have been performed for $Gd_{11}Ni_4In_9$ [4], $Tb_{11}Ni_4In_9$ and $Dy_{11}Ni_4In_9$ [5]. Expectedly, electrical resistivity and magnetism of these compounds are strongly anisotropic. Interesting and vastly different magnetic behaviors have been observed depending on the orientation of the fibers with respect to the magnetic field vector, **H**: upon lowering the temperature, multiple ferrimagnetic orderings are detected when the fibers are oriented parallel to **H** (along the c-axis, which is both the easy-magnetization and high electrical-conductivity direction), while an antiferromagnetic ground state is observed when the fibers are oriented orthogonal to **H** (in the *ab*-plane). Field induced metamagnetic transitions and evidence of Griffiths-like phase have also been reported. Heat capacity and magnetic properties of $R_{11}Ni_4In_9$ compounds (for R = Pr, Nd, Sm, Gd and Tb [7], Ce [8] and Dy [9]) were measured recently; these measurements, however, have been performed on non-oriented specimens.

The $R_5Ni_2In_4$ compounds ($m = 4$, $n = 1$) crystallize in the $Lu_5Ni_2In_4$-type structure [10] (orthorhombic *oP*22, *Pbam*, $Z = 2$) for R = Tb-Tm, Lu, Y and Sc [10–14]. Though close in composition to $R_{11}Ni_4In_9$, i.e. '$R_{10}Ni_4In_8$', these compounds, however, do not solidify in a similar microfibrous morphology. Magnetic susceptibility measurements on $Ho_5Ni_2In_4$ were given as a short report in [15], while the magnetic properties of $Er_5Ni_2In_4$ and $Tm_5Ni_2In_4$ were reported in [13] and [16], respectively.

In this article, we report on the magnetic properties and magnetic structures of the $R_5Ni_2In_4$ and $R_{11}Ni_4In_9$ compounds with R = Tb and Ho as deduced from magnetization, heat capacity, and neutron diffraction data. We note that there are five and three symmetrically inequivalent rare earth sites in $R_{11}Ni_4In_9$ and $R_5Ni_2In_4$ compounds, respectively. As a result the intra- and inter-magnetic interactions, mediated by the indirect RKKY exchange interactions, can be different at different rare earth sites; this leading in principle to a cascade of magnetic transitions. The crystal electric field due to the neighbouring charges and experienced by the symmetry in-equivalent rare earth ions can also vary, which may, for example, vary the magnetocrystalline anisotropy (MCA) of the rare earth ions. Among other factors, the MCA decides the easy-magnetization axis in rare earth compounds.

2. Experimental

Samples (total mass of 8–10 g), with nominal composition $R_5Ni_2In_4$ and $R_{11}Ni_4In_9$, were prepared for R = Tb, and Ho. The starting metals were high purity Tb and Ho (99.9 + wt.% pure with respect to all other elements in the periodic table) obtained from the Materials Preparation Center of the Ames Laboratory [17] and commercial Ni (99.99 wt.% purity) and In (99.999 wt.% purity). The alloys were prepared by arc melting the elements under a pure argon atmosphere; the buttons were re-melted three times turning them upside-down each time to ensure homogenization. Weight losses were between 0.2–0.5 wt.%. The ingots were wrapped in Ta foil, sealed under vacuum in silica tubes and annealed at 1000 °C for 7–14 d. Powders were prepared by grinding in an agate mortar in Ar atmosphere; for the fibrous $Tb_{11}Ni_4In_9$ and $Ho_{11}Ni_4In_9$ alloys, ground samples were further annealed at 400 °C for 7 d. Phase analysis was performed by x-ray powder diffraction, using a Guinier camera (Cu Kα_1 radiation; Si as internal standard); the analysis showed the samples to be single phase.

The powder neutron diffraction data were recorded at the Institut Laue Langevin (Grenoble) on the high resolution powder diffractometer D2B with $\lambda = 1.594$ Å at room temperature and for the two $R_{11}Ni_4In_9$ compounds at selected temperatures down to 2 K using the high intensity diffractometer D1B using $\lambda = 2.52$ Å. The neutron powder diffraction patterns as function of temperature (thermodiffractogram) were collected on D1B for $Ho_5Ni_2In_4$ between 2 K and 35 K and for $Ho_{11}Ni_4In_9$ between 2 K and 26 K recording the data for 10 min every 1 K. $Tb_5Ni_2In_4$was measured between 2 K and 160 K with a ΔT of 1.2 K, while the $Tb_{11}Ni_4In_9$ spectra were recorded for 10 min every 1.2 K between 2 K and 50 K and then every 3.2 K between 50 K and 150 K. For the measurement of $Ho_5Ni_2In_4$, the cryostat was slightly rotated from its ideal position in order to access the lowest possible Bragg angles, thereby creating additional scattering from its aluminum tail. All neutron data were analyzed using the Rietveld refinement program FULLPROF [18]. Sketches of the crystallographic and magnetic structures were drawn with the program FullProf Studio [18].

Heat capacity data were collected using an automated semiadiabatic calorimeter from 2 to 300 K and in magnetic fields of 0, 10 and 20 kOe [19]. The DC magnetization as a function of both temperature (in the range 2–300 K) and applied magnetic field was measured in a magnetic property measurement system (MPMS, Quantum Design) and a physical property measurement system (PPMS, Quantum Design), up to 70 kOe.

3. Results and discussion

3.1. Heat capacity and magnetization measurements

3.1.1. $Tb_5Ni_2In_4$. The heat capacity of $Tb_5Ni_2In_4$ has been measured between 2 and 350 K in zero and applied fields of 10 and 20 kOe (figures 1(a)–(c)). The data show two peaks at about 120 K and 19.5 K, followed by two weak anomalies at 11 K and 8 K. The high temperature main peak at 120 K broadens and shifts to higher temperatures with increasing magnetic field, thus suggesting a ferro/ferrimagnetic transition (figure 1(a)). The second and weaker peak at 19.5 K moves slightly to lower temperatures in applied magnetic field, indicating an antiferromagnetic like ordering around this temperature (figure 1(b)). Both of these anomalies are in agreement with the detailed neutron diffraction data (*vide infra*). The two remaining minor anomalies at 11 and 8 K apparently move to lower temperatures in applied magnetic fields; however, the neutron data do not show any evidence of magnetic transitions at these two temperatures. Their origin remains unknown at present; we tentatively attribute them to unknown trace magnetic impurity phase(s). They do not appear to be due to either $Tb_{11}Ni_4In_9$ (which shows $T_C = 112$ K and two more transitions at 31 and 21 K) or TbNiIn (which orders antiferromagnetically at $T_N = 68$ K, with a second transition at 26 K [20]).

The DC magnetization of $Tb_5Ni_2In_4$ measured as a function of temperature is shown in figure 2(a). The Curie-Weiss [$\chi = C_{CW}/(T - \theta_P)$] fit of the data between 200 and 300 K (figure 2(a), inset) yields an effective magnetic moment $\mu_{eff} = 9.15\ \mu_B$ ($9.22\ \mu_B$ from data at 20 kOe) and a Weiss temperature $\theta_P = 87.8$ K. The value of the effective magnetic moment is slightly lower than the theoretical value of $9.72\ \mu_B$ for the free Tb^{3+} ion [21]; the positive value of the Weiss temperature suggests a ferro/ferrimagnetic ground state, which is consistent with the heat capacity results shown in figure 1(a). The M/H versus T plots reveal a paramagnetic to a ferro or ferrimagnetic transition. A peak in the first derivative of the field cooling (FC) data at 1 kOe establishes a Curie temperature, T_C, of 121 K, in excellent agreement with the heat capacity (*vide supra*) and neutron diffraction (*vide infra*) data; the peak shifts to 128 K in an applied field of 20 kOe. Unlike $Ho_5Ni_2In_4$ (*vide infra*), the magnetization of $Tb_5Ni_2In_4$ shows irreversible thermomagnetic behavior between zero field cooled (ZFC) heating and FC conditions starting from about 70 K at 1 kOe and 20 K at 20 kOe. A comparison of the ZFC and FC plots in 1 kOe suggests that the ferro/ferrimagnetic state has a sizeable coercive field, arising most likely from single-ion anisotropy. As the applied field is increased such that it becomes comparable to the (temperature dependent) coercive field, the irreversibility between the ZFC and FC plots decreases. The peak near 20 K in the 20 kOe data is due to the antiferromagnetic ordering of one of the three independent Tb sites present in this structure as detected in the neutron diffraction data (*vide infra*). The competition between the ferro/ferrimagnetic and the antiferromagnetic exchange interactions intrinsic to various Tb sites explains why θ_p (87.8 K) is substantially lower than T_C (121 K) in this compound. The magnetic behavior of this compound is similar to the one observed for $Dy_5Ni_2In_4$ [11].

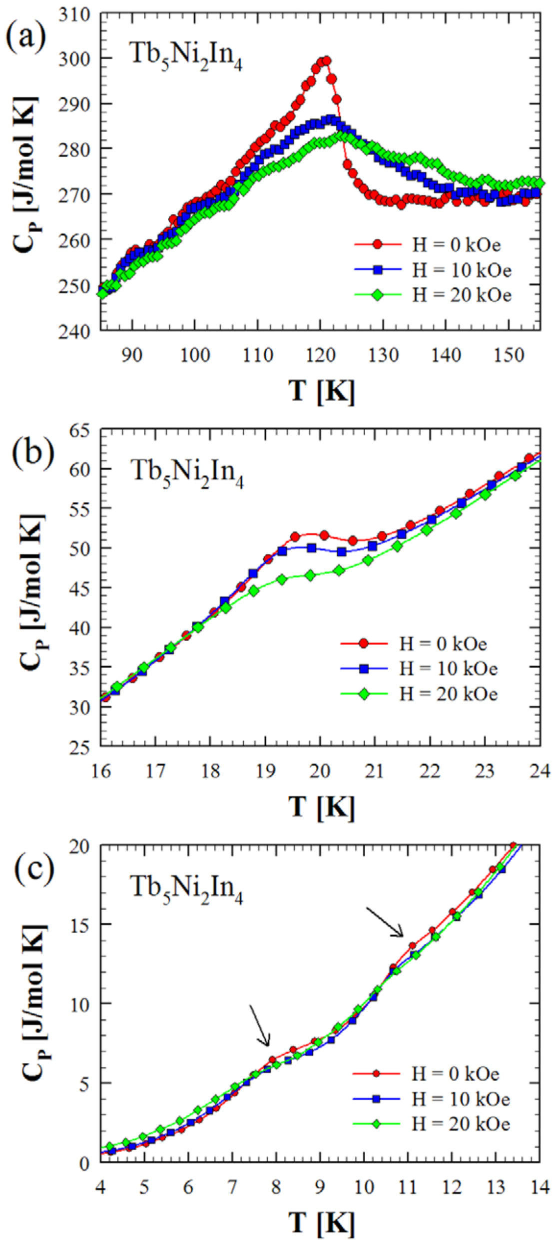

Figure 1. Heat capacity of $Tb_5Ni_2In_4$ measured in applied magnetic fields of 0, 10 and 20 kOe; (a), (b), and (c) show the data between 85 and 155 K, 16 and 24 K, and 4 and 14 K, respectively.

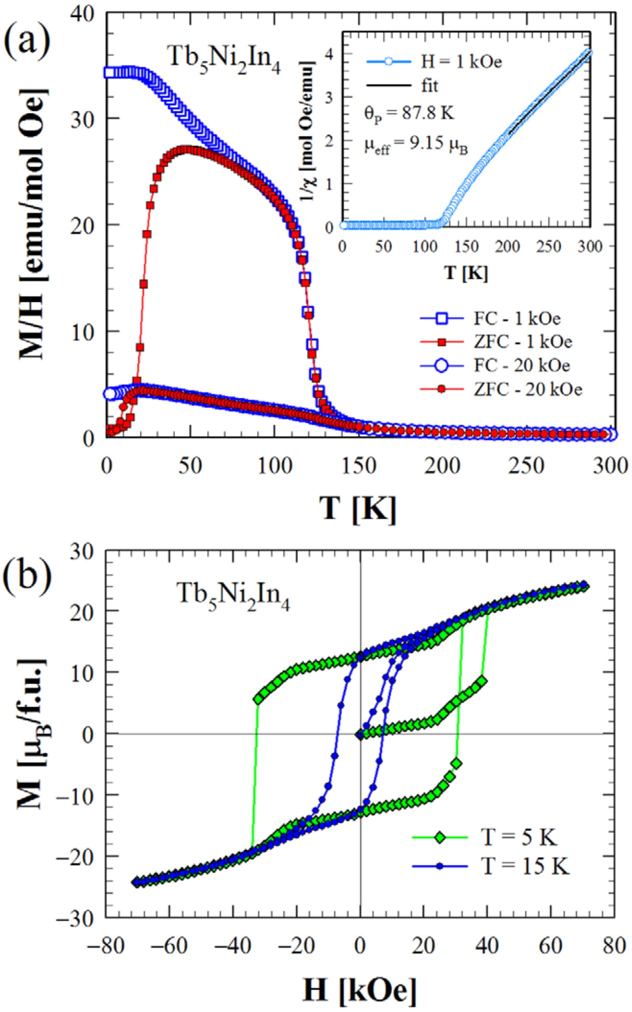

Figure 2. (a) Magnetic susceptibility (M/H) of $Tb_5Ni_2In_4$ versus temperature measured between 2 and 300 K in applied magnetic fields of 1 kOe and 20 kOe; the inset shows the inverse magnetic susceptibility (H/M) for 1 kOe magnetic field and the Curie-Weiss fit. (b) Isothermal magnetization of $Tb_5Ni_2In_4$ measured at 2 K and 15 K.

The isothermal magnetization of $Tb_5Ni_2In_4$ measured at 2 and 15 K is shown in figure 2(b). Similar to $Dy_5Ni_2In_4$ [11], $Tb_5Ni_2In_4$ shows a wide hysteresis loop at 2 K, with a coercive field, H_C, as high as ≈30 kOe. Here, H_C is also similar to the values found in $Tb_{11}Ni_4In_9$ and $Dy_{11}Ni_4In_9$ [5]. The M(H) data at $T = 2$ K also indicate a metamagnetic transition at ≈25 kOe. At 15 K, the metamagnetic transition is no longer evident and the hysteresis loop becomes narrower (figure 2(b)).

3.1.2. $Ho_5Ni_2In_4$. The heat capacity, C_P, of $Ho_5Ni_2In_4$ is shown in figure 3. The peak around 31 K corresponds to the onset of antiferromagnetic transition as detected by neutron diffraction (*vide infra*). A minor anomaly near 18 K, seen more prominently in the C_P/T *versus* T^2 plot (figure 3, inset), is followed by a peak near 4 K. The anomaly at 18 K can be related to the change of the magnetic structure from antiferromagnetic to ferromagnetic state as observed in the neutron diffraction results at about 20 K, whereas the anomaly at 4 K most probably arises due to the magnetic coupling of the Ho2 site with the other Ho sites (*vide infra*).

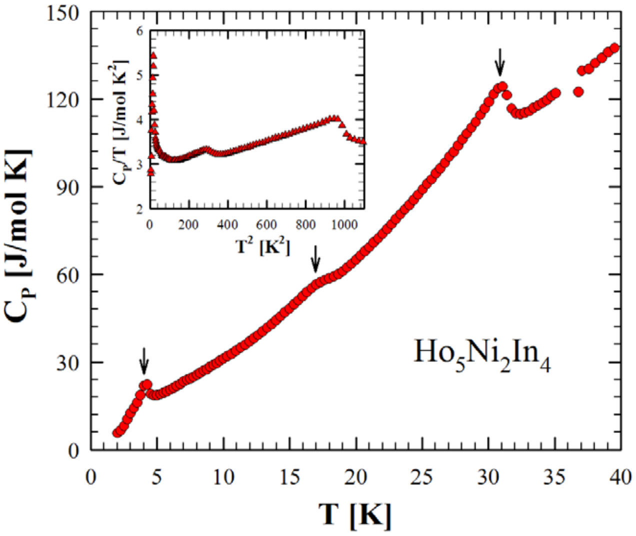

Figure 3. Heat capacity of $Ho_5Ni_2In_4$ between 2 and 40 K with the anomalies indicated by arrows. The single data point anomaly around 37 K is an experimental artefact. The inset shows the C_P/T versus T^2 data between 0 and ~34 K.

The temperature dependence of the DC magnetization for $Ho_5Ni_2In_4$ was measured between 2 and 300 K in applied magnetic fields of 1 and 20 kOe (figure 4(a)). The Curie-Weiss fit of the data between 50 K and 300 K (figure 4(a), inset) yields an effective magnetic moment $\mu_{eff} = 10.51$ μ_B and a Weiss temperature $\theta_P = 25.7$ K. The value of the effective magnetic moment is close to the theoretical value of 10.61 μ_B for the free Ho^{3+} ion [21]; this good agreement also indicates that Ni ions are non-magnetic in this compound and the Ni 3*d*-band fully filled [4, 5, 11]. The positive value of the paramagnetic Curie temperature *prima-facie* indicates a ferro/ferrimagnetic ground state. Neutron data show the onset of an antiferromagnetic transition at 31 K which is gradually suppressed and replaced by a ferromagnetic configuration beginning at 25 K (*vide infra*). An almost reversible thermomagnetic behavior is observed between the FC and ZFC magnetization at both 1 and 20 kOe (main panel, figure 4(a)); however, a careful examination shows that the ZFC plot exhibits a downturn below ≈4 K. The magnetization data at 1 kOe reveal a rapid upturn around 32 K [as inferred from the first derivative dM(*T*)/d*T* of the FC data], however the cusp typical for an antiferromagnetic transition is not observed, and most likely due to the proximity of the ferromagnetic transition at lower temperatures. The upturn broadens and the first derivative dM(*T*)/d*T* shifts upwards by nearly 25 K in the higher field of 20 kOe.

The isothermal magnetization, at selected temperatures between 2 and 40 K, is shown in figure 4(b). At 40 K, above $T_N = 31$ K, the magnetization does not vary linearly with field, presumably because of the short-range magnetic correlations in the vicinity of T_N (it may be noted that in figure 4(a) the upturn in the magnetization in a field of 1 kOe begins around 40 K). As the temperature is lowered, the shape of the plots remains similar, except that the magnetization increases and a sharp ferromagnetic-like increase at low fields also increases with decreasing temperature. The coercive field at 2 K is about 1 kOe, which may explain the downturn in the ZFC plot

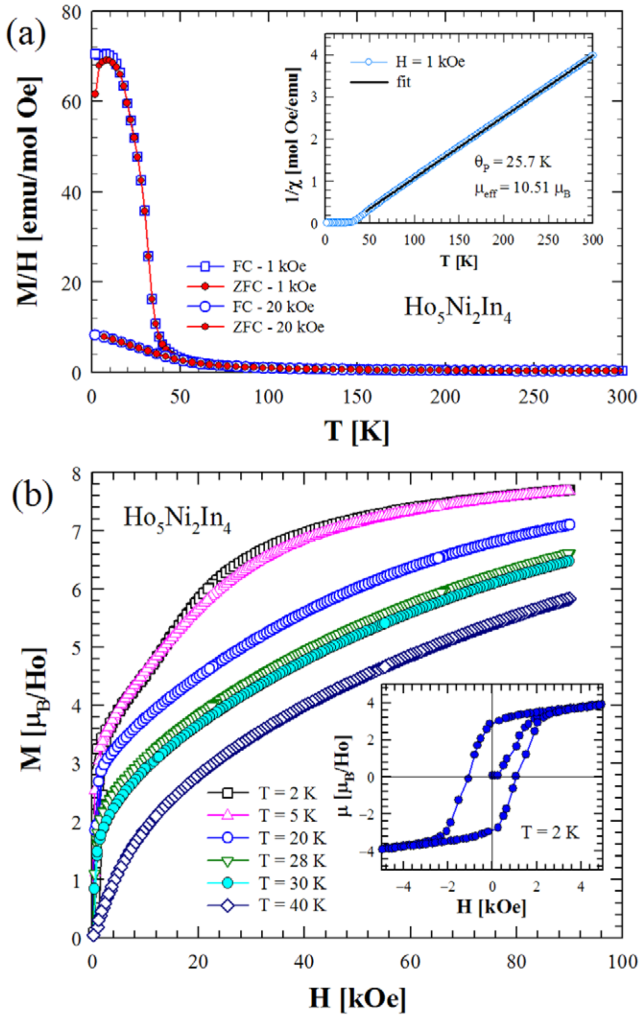

Figure 4. (a) Magnetic susceptibility (M/H) of $Ho_5Ni_2In_4$ versus temperature measured between 2 and 300 K in applied magnetic fields of 1 kOe and 20 kOe; the inset shows the inverse magnetic susceptibility measured in 1 kOe. (b) Isothermal magnetization of $Ho_5Ni_2In_4$, measured at several temperatures in field of up to 90 kOe; the inset displays the hysteresis loop measured at 2 K.

below ≈5 K measured at 1 kOe (figure 4(a)). The magnetization does not reach saturation at 90 kOe, most likely due to the ferrimagnetic arrangement of the Ho2-sublattice with the rest of the Ho ions (see figure 9(b)).

3.1.3. $Tb_{11}Ni_4In_9$. The magnetic properties of $Tb_{11}Ni_4In_9$ along with those for the light *R* have been reported by Szytula *et al* [7]; more recently, the physical properties of $Tb_{11}Ni_4In_9$ and $Dy_{11}Ni_4In_9$ have been investigated in more details and on oriented microfibers [5]. A complex magnetic behavior with multiple magnetic transitions has been found in $Tb_{11}Ni_4In_9$, with the first ordering at $T_C = 112$ K, which is followed by two other transitions at 31 K and 23 K. Ferrimagnetic-like behavior, with extremely high coercive fields ($H_C = 6.6$ T at 5 K) is found when the fibers are parallel to the magnetic field direction (oriented parallel to the *c*-axis); an antiferromagnetic-like response is observed with the fibers oriented orthogonal (i.e. in the *a*-*b* plane). Induced spin-flop magnetic transitions and the appearance of a Griffiths phase regime (before entering the ordered magnetic states) were also reported [5].

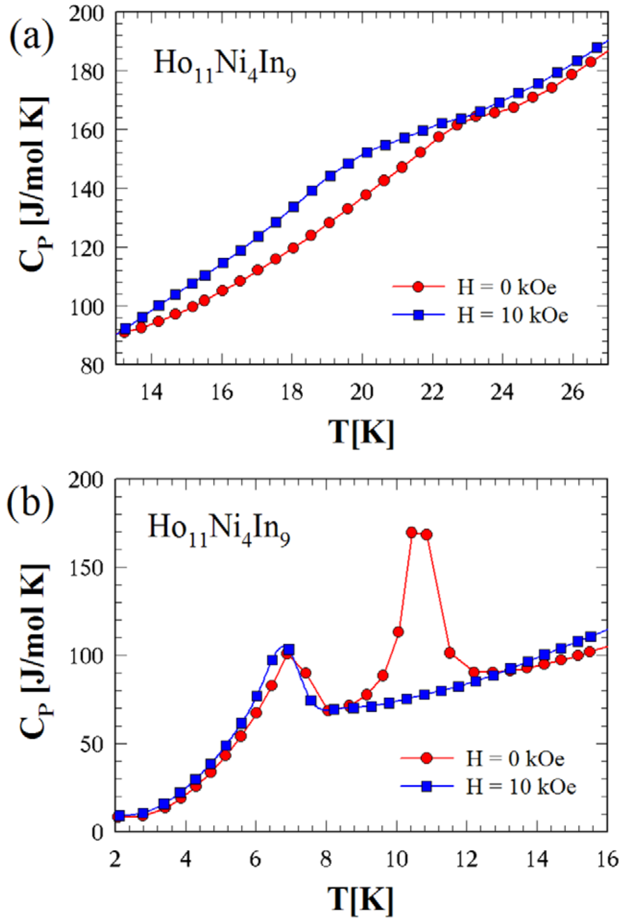

Figure 5. Heat capacity of $Ho_{11}Ni_4In_9$ measured in applied magnetic fields of 0 and 10 kOe; (a) shows the data between 13 and 27 K and (b) shows the data between 2 and 16 K.

3.1.4. $Ho_{11}Ni_4In_9$. The heat capacity of $Ho_{11}Ni_4In_9$ was measured between 1.8 and 300 K in zero and applied magnetic fields of 10 kOe. The data between 13–27 K and 2–16 K are shown in figures 5(a) and (b), respectively. The zero field data reveal the presence of at least three anomalies: traversing down from high temperature, a first weak and broad peak at 23 K is followed by two sharp peaks at 10.5 K and 7 K. In the applied magnetic field (10 kOe), both the first and the third anomaly slightly move to lower temperature, suggesting antiferromagnetic-type magnetic transitions. Interestingly, the peak at 10.5 K completely disappears in applied magnetic field of 10 kOe (figure 5(b)), some additional comments regarding the disappearance are found in section 3.2.4.

The magnetic measurements on $Ho_{11}Ni_4In_9$ were not performed with fibers oriented perpendicular and parallel to **H**, rather a small piece of appropriate mass was cut randomly from the alloy button and loaded into the magnetometer. The DC magnetization was measured in applied magnetic fields of 500 Oe and 25 kOe in both ZFC and FC modes; the data are plotted in figures 6(a). The inverse magnetic susceptibility, $1/\chi$, (inset in figure 6(a)) follows the Curie-Weiss law; the linear fit in

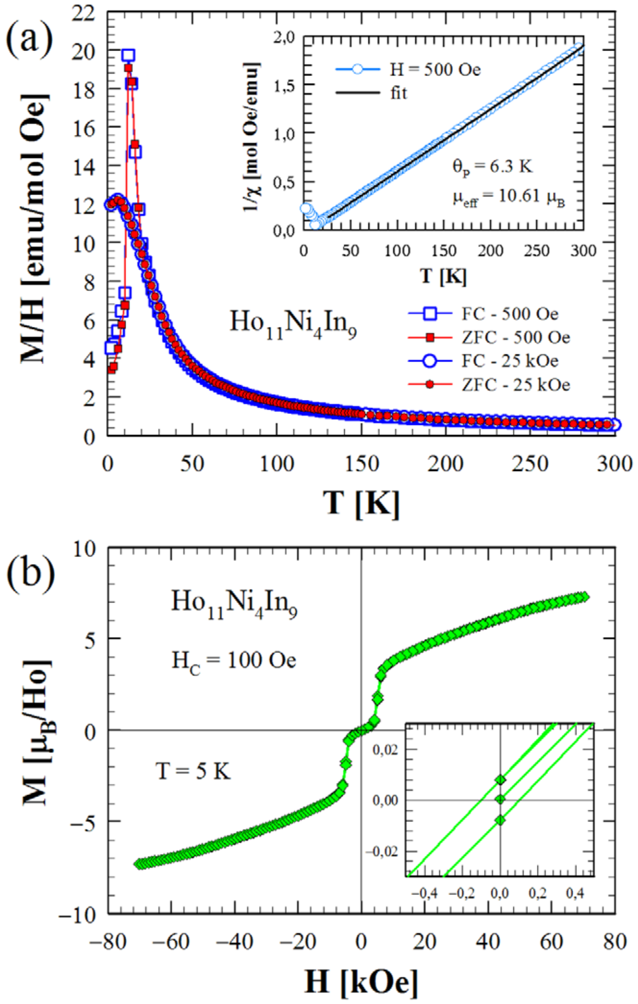

Figure 6. (a) Magnetic susceptibility (M/H) versus temperature of $Ho_{11}Ni_4In_9$ measured between 2 and 300 K in applied magnetic fields of 500 Oe and 25 kOe; the inset shows the $1/\chi$ plot for the measurements at 500 Oe. (b) Isothermal magnetization of $Ho_{11}Ni_4In_9$ measured at 5 K; the inset is a blow-up of the magnetization near $H = 0$ kOe.

the temperature range 25–300 K yields an effective magnetic moment $\mu_{\mathrm{eff}} = 10.61\ \mu_B$ and a Weiss temperature $\theta_P = 6.3$ K. The magnetic moment is identical to the theoretical value for the free Ho^{3+} ion [21]; the low value of θ_P suggests a relatively weak exchange interaction(s) in this compound. Neutron data show a cascade of four antiferromagnetic transitions, the highest one occurring at 22 K (*vide infra*). Therefore, the positive value of θ_P may be due to the crystal electric field effects. The ZFC and FC magnetization plots (main panel figure 6(a)) do not show any thermomagnetic irreversibility. This is in agreement with the neutron scattering data. The magnetization data at 500 Oe show a peak at around 13 K, suggesting an antiferromagnetic behavior in this compound. When the field is increased to 25 kOe the peak is shifted down to ≈ 5 K and the magnetic susceptibility decreases by about a third. This suggests that the magnetic field has a strong effect on the cascade of antiferromagnetic transitions in this compound. The isothermal magnetization was measured at 5 K up to 70 kOe (figure 6(b)). The data show one clear metamagnetic transition at about 5 kOe and the magnetization does not saturate up to 70 kOe. Surprisingly, a narrow hysteresis is observed with a coercive field of ≈100 Oe.

Table 1. Results of the Rietveld refinement of the high resolution neutron diffraction data for $R_5Ni_2In_4$ with R = Ho, Tb.

R		Ho (300 K)	Tb (130 K)
$R1$ (2a)			
$R2$ (4g)	x	0.2206(2)	0.2220(2)
	y	0.2429(6)	0.2456(5)
$R3$ (4g)	x	0.4150(3)	0.4157(2)
	y	0.1202(4)	0.1187(4)
Ni (4h)	x	0.3037(2)	0.3050(2)
	y	0.0263(4)	0.0258(4)
In1 (4h)	x	0.5700(5)	0.5711(4)
	y	0.2013(11)	0.2070(9)
In2 (4h)	x	0.8489(5)	0.8471(4)
	y	0.0713(11)	0.0705(9)
a		17.7823(6)	17.8932(5)
b		7.8862(3)	7.9074(3)
c		3.5735(1)	3.5943(1)
R_{Bragg}		8.1	6.4

3.2. Neutron diffraction

3.2.1. $Ho_5Ni_2In_4$. High resolution data taken on the D2B diffractometer at room temperature confirm that $Ho_5Ni_2In_4$ crystallizes in the $Lu_5Ni_2In_4$-type (space group *Pbam*); crystallographic details are given in table 1. The sample is pure apart from a minor impurity phase (about 2%) of HoNiIn [22]. Figure 7(a) displays the thermal dependence of the neutron diffraction intensity in the low Bragg angle region measured on the high intensity diffractometer D1B between 2 K and 35 K.

New Bragg peaks of magnetic origin appear below about $T_N = 31$ K. Further cooling leads, however, to the near disappearance of these peaks starting from about $T_C = 20$ K together with the simultaneous increase of peaks situated at nuclear Bragg peak positions. Both sets of magnetic peaks can be indexed with the magnetic propagation vector $\kappa = (0, 0, 0)$. Figure 7(b) shows the temperature dependence of the (1 0 0) and the (2 0 0) peaks which are representative of the two different magnetic phases.

Magnetic symmetry analysis using the program BASIREPS [23, 24] gives the allowed irreducible representations (IR) and their basis vectors (BV) for the two different Ho Wykoff positions (Ho1 on Wyckoff site 2a, Ho2 and Ho3 on Wyckoff site 4g in the space group *Pbam*) with $\kappa = (0, 0, 0)$; see table 2.

In order to achieve a higher sensitivity for the magnetic scattering intensity, difference spectra, where the nuclear scattering was subtracted using data measured above T_N, were generated. No magnetic contribution from the small impurity phase of HoNiIn, which becomes ferromagnetic below 22 K [22], is visible. A scale factor was determined from the refinement of the purely nuclear scattering data taken at $T = 35$ K with the atomic coordinates fixed to the values as determined from the high resolution data. Due to the appearance of new magnetic peaks only those IR's having an antiferromagnetic

Table 2. Basis vectors (BV) of the allowed irreducible representations (IR) for $\kappa = (0, 0, 0)$ for the Wyckoff positions 2*a* and 4*g* of space group *Pbam* occupied by the rare earth (*R*) in $R_5Ni_2In_4$ compounds; refined values of the coefficients of the BV's and magnetic moment values for $Ho_5Ni_2In_4$ at 25 K and 2 K and for $Tb_5Ni_2In_4$ at 50 K, 20 K and 2 K following $\kappa = (0, 0, 0)$. Refer to table 3 for the additional order present in $Tb_5Ni_2In_4$ at 2 K with $\kappa = (0, \delta, ½)$ and the resulting total magnetic moments for the three Tb sites.

	IR1	IR2		IR3	IR4		IR5		IR6	IR7		IR8		
$\kappa = [0\ 0\ 0]$	BV1	BV1	BV2	BV1	BV1	BV2	BV1	BV2	BV1	BV1	BV2	BV1		
R (2a) x, y, z	0 0 1			0 0 1			1 0 0	0 1 0		1 0 0	0 1 0			
$-x + ½, y + ½, -z$	0 0 −1			0 0 1			−1 0 0	0 1 0		1 0 0	0 −1 0			
R (4 g) x, y, z	0 0 1	1 0 0	0 1 0	0 0 1	1 0 0	0 1 0	1 0 0	0 1 0	0 0 1	1 0 0	0 1 0	0 0 1		
$-x, -y, z$	0 0 1	−1 0 0	0 −1 0	0 0 1	−1 0 0	0 −1 0	1 0 0	0 1 0	0 0 −1	1 0 0	0 1 0	0 0 −1		
$-x + ½, y + ½, -z$	0 0 −1	−1 0 0	0 1 0	0 0 1	1 0 0	0 −1 0	−1 0 0	0 1 0	0 0 −1	1 0 0	0 −1 0	0 0 1		
$x + ½, -y + ½, -z$	0 0 −1	1 0 0	0 −1 0	0 0 1	−1 0 0	0 1 0	−1 0 0	0 1 0	0 0 1	1 0 0	0 −1 0	0 0 −1		
$Ho_5Ni_2In_4$													$\mu_R[\mu_B]$	R_{Mag}
25 K														10.6
Ho1	−5.2(1)						−1.7						5.5(1)	
Ho2	0						0						0	
Ho3	2.0(1)						1.1(3)						2.2(2)	
2K														11.3
Ho1				7.6(1)						3.1(4)			8.2(1)	
Ho2				0						−1.2(2)			1.2(2)	
Ho3				5.8(1)						2.8(3)			6.4(2)	
$Tb_5Ni_2In_4$														
50 K														7.6
Tb1				8.0(1)									8.0(1)	
Tb2				0									0	
Tb3				6.4(1)									6.4(1)	
20 K														6.0
Tb1				8.3(1)						1.1(1)			8.4(1)	
Tb2				0						0			0	
Tb3				8.0(1)						−1.1(1)			8.1(1)	
2K														5.8
Tb1				7.9(1)						1.0(1)			8.0(1)	
Tb2				0						0			0	
Tb3				7.9(1)						−1.0(1)			8.0(1)	

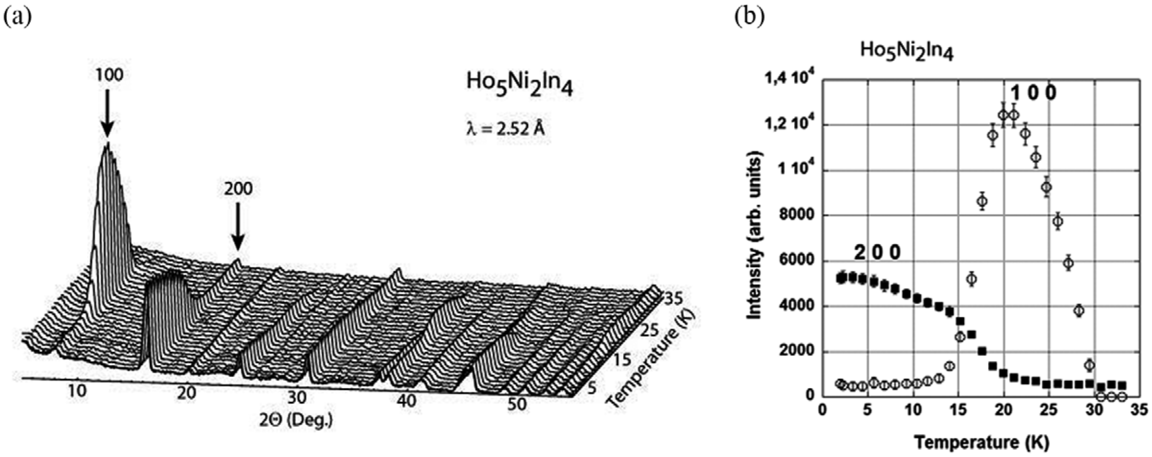

Figure 7. (a) Thermodiffractogram of $Ho_5Ni_2In_4$; (b) T-dependence of the (100) and the (200) reflections representative for the two magnetic phases.

alignment between magnetic spins within the unit cell can account for the magnetic phase present below 31 K. This excludes e.g. IR3 and BV2 of IR5 and BV1 of IR7. Testing the different allowed antiferromagnetic arrangements it turned out that only a combination of IR1 and BV1 of IR5 was able to reproduce the measured magnetic intensities. Figure 8(a) shows the refinement of the pure magnetic scattering intensity at $T = 25$ K, e.g. above the onset of the second magnetic transition, while figure 8(b) displays the resulting magnetic structure; table 2 contains the refined magnetic moment values.

Layers of ferromagnetically aligned spins of Ho1 and Ho3 within the (1 0 0) plane are antiferromagnetically coupled to those shifted by $a/2$. The sublattices of Ho1 and Ho3 are nearly parallel having a large component in the c-direction, with only a small canting towards the a-direction. The magnetic moment of the Ho1 site is significantly larger than that of the Ho3 site with no magnetic moment on the Ho2 site (which is situated between the antiferromagnetically coupled layers). As already mentioned above, this magnetic structure disappears nearly completely on further cooling, and gets replaced by a different magnetic structure.

The new magnetic structure obtained by refining the difference data 2 K–35 K (figure 9(a)) was found to conform to IR3 and BV1 of IR7, leading to a purely ferromagnetic alignment of spins on Ho1 and Ho3 as shown in figure 9(b), with the spins pointing again mostly in the c-direction. A small magnetic moment aligned ferrimagnetically to Ho1 and Ho3 in the a-direction is now detectable as well on the Ho2 site; table 2 lists the details of the refined magnetic moment values.

The refinement shown in figure 9(a) is in fact a 2-phase refinement as the high temperature antiferromagnetic phase is still present in small amounts at 2 K. This is most easily seen by the presence of the (1 0 0) reflection at $2\Theta \approx 6°$. Assuming that the magnetic moments at 2 K of the antiferromagnetic phase are similar in magnitude to their peak values found at ≈20 K (see figure 7(b)), the concentration of this minority magnetic phase at 2 K can be determined to be about 5 wt.%. A small feature around $2\Theta = 22°$, which appears in the diffraction data only at the lowest measured temperature $T = 2$ K and which is not accounted for by the refinement shown in figure 9(a), has to be connected to the establishment of an additional magnetic order (probably involving mostly the Ho2 site) similar to the situation in $Tb_5Ni_2In_4$ as will be explained below. It should be linked to the anomaly seen at about 4 K in the heat capacity data (see figure 4).

3.2.2. $Tb_5Ni_2In_4$. High resolution data taken at 130 K confirm the structural prototype (space group *Pbam*) and the phase purity of $Tb_5Ni_2In_4$. The crystallographic details are included in table 1. Figure 10(a) shows the thermodiffractogram between 2 K and 160 K of this compound. A magnetic contribution to the diffraction pattern becomes first visible at about $T_C = 125$ K; however, a second magnetic transition is indicated at around $T_N = 20$ K by the appearance of additional reflections. Above 20 K all magnetic peaks can be indexed by the magnetic propagation vector $\kappa_1 = (0, 0, 0)$; figure 10(b) shows that the temperature dependence of the (2 0 0) and (1 1 0) peaks is non-uniform, reflecting the different temperature dependencies of the magnetic ordering on the independent Tb sites.

In the following all refinements were done on the purely magnetic scattering intensity using the difference patterns created by subtracting the nuclear scattering of a data set taken within the paramagnetic region at 130 K. Fixing the atomic coordinates to the values determined from the high resolution data this paramagnetic data set was first refined in order to determine the scale factor needed to refine the purely magnetic data sets. Since the magnetic propagation vector is the same as in the case of $Ho_5Ni_2In_4$, one can use the symmetry restrictions listed in table 2 to determine the magnetic structure of $Tb_5Ni_2In_4$. It turns out that in the temperature range $30\,K \leqslant T < T_C$ the magnetic structure is simple ferromagnetic along the c-direction following IR3 for the Tb1 and the Tb3 sites, while no magnetic moment can be detected on the Tb2 site. A cyclic refinement of the data (figure 11(a)) shows that the two Tb-sublattices follow strongly differing temperature dependences with the magnetic moment on the Tb1 site increasing rapidly below T_C and then rapidly approaching saturation, while the Tb3 site magnetic moment increases nearly linearly on cooling. These two different trends determine the

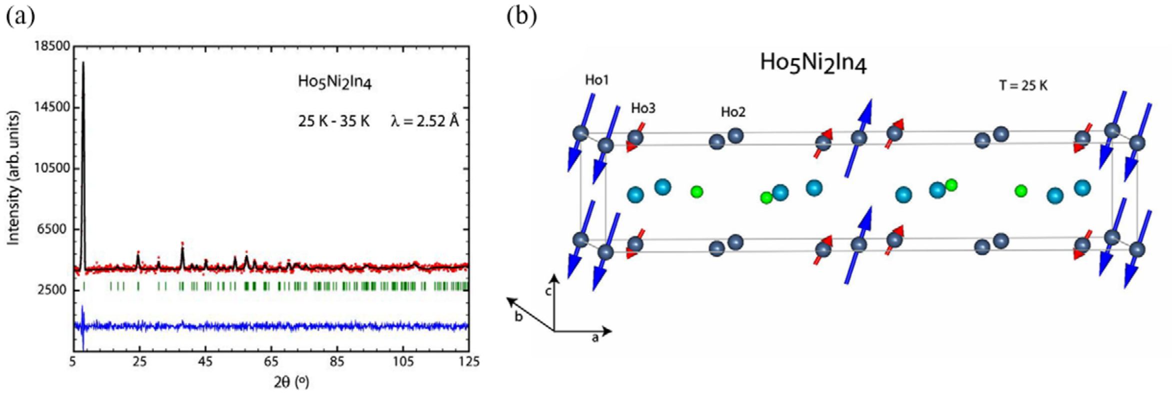

Figure 8. (a) Observed (dots, red), calculated (line, black) and difference pattern of the (25 K–35 K) data of $Ho_5Ni_2In_4$ with nuclear scattering subtracted off. The tick marks indicate the calculated position of the magnetic Bragg peaks. (b) Magnetic structure of $Ho_5Ni_2In_4$ at 25 K; small green (light blue) balls represent the Ni (In) atoms.

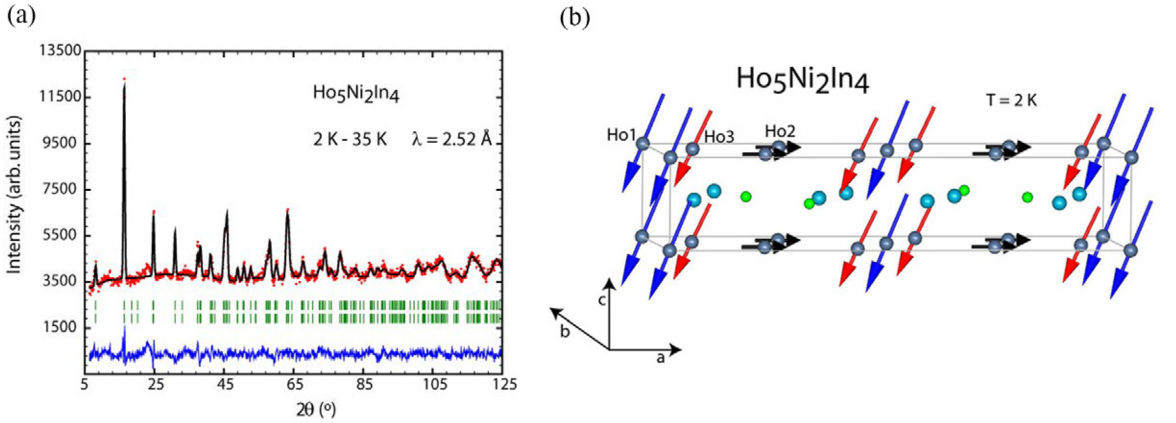

Figure 9. (a) Refinement of the difference spectrum 2 K–35 K of $Ho_5Ni_2In_4$. Observed (dots, red), calculated (line, black) and difference pattern. The tick marks indicate the calculated positions of the magnetic Bragg peaks of the main phase and of the minority phase. (b) Magnetic structure of $Ho_5Ni_2In_4$ at 2 K; small green (light blue) balls represent the Ni (In) atoms. The size of the Ho2 magnetic moment has been exaggerated in the figure to facilitate its representation.

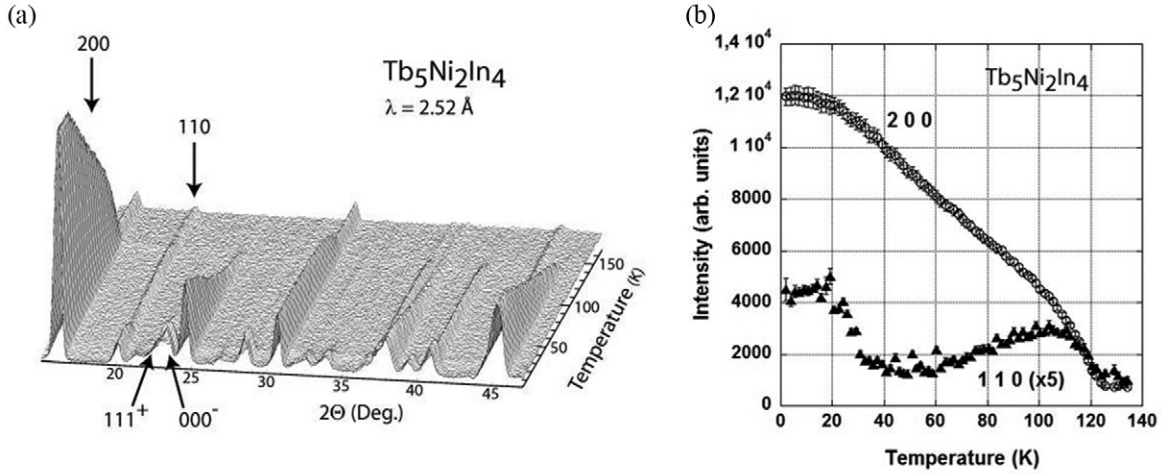

Figure 10. (a) Thermodiffractogram of $Tb_5Ni_2In_4$. (b) T-dependence of the (2 0 0) and the (1 1 0) reflections.

non-uniform behavior of the (1 1 0) reflection (figure 10(b)) between T_C and 30 K. Below 30 K an additional magnetic component in the *a*-direction sets in (BV1 of IR7) for the Tb1 and Tb3 sites (figure 11(a)) leading to a slight reorientation of the ferromagnetic spin direction and to a re-increase of the (1 1 0) reflection.

The components in the *a*-direction of the Tb1 and Tb3 sublattices are ferrimagnetically aligned; as they are equal within the error bars, they were fixed in the refinements to the same absolute value. Table 2 lists the refined magnetic moment values for $T = 50$ K and 20 K. Figure11(b) shows the fit of the purely magnetic scattering at 50 K, while figure 12(a) depicts the magnetic structure at 20 K.

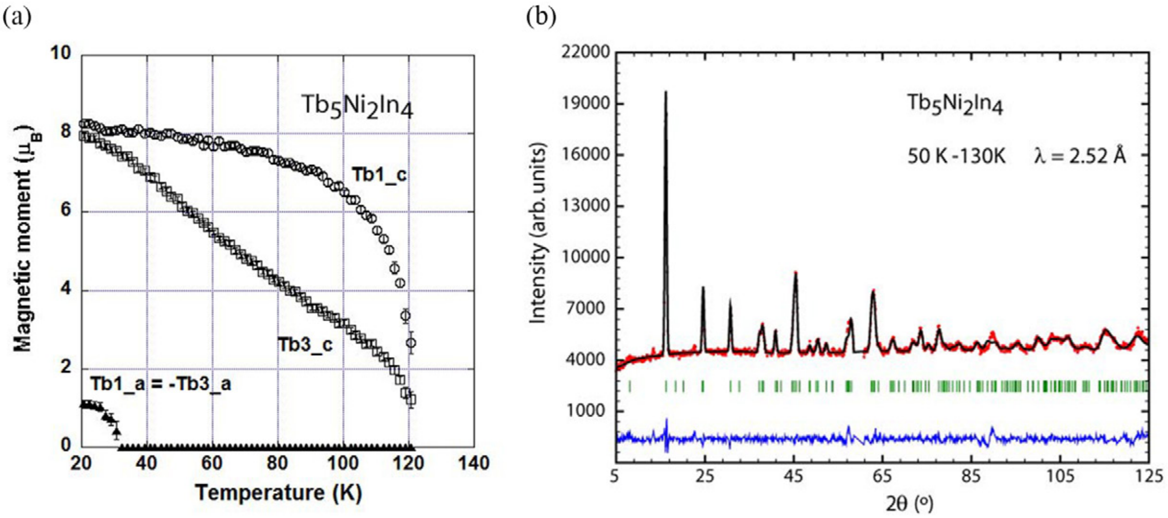

Figure 11. (a) Ferromagnetic components in *c*- and *a*-direction for Tb1 and Tb3 sublattices in the ferromagnetic phase of $Tb_5Ni_2In_4$ between 20 K and T_C. (b) Observed (dots, red), calculated (line, black) and difference pattern of the (50 K–130 K) data of $Tb_5Ni_2In_4$.

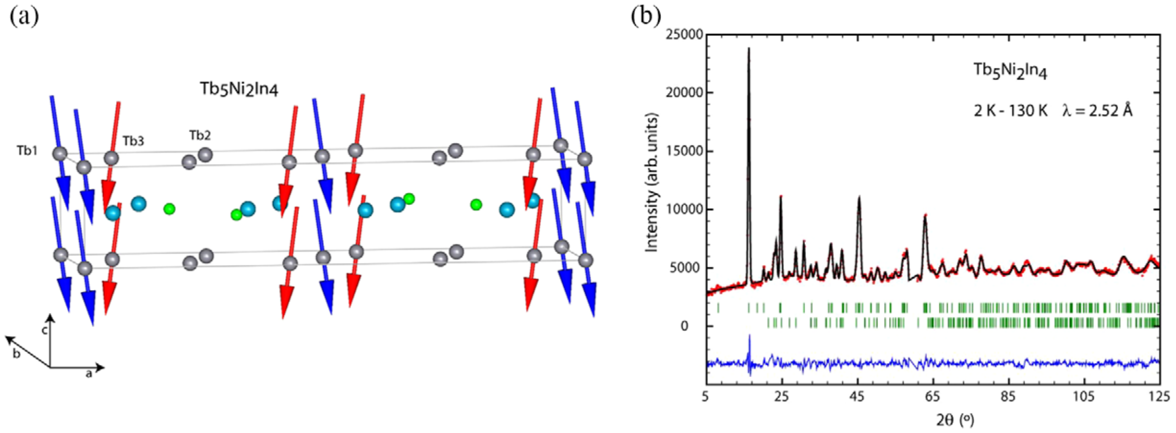

Figure 12. (a) Magnetic structure of $Tb_5Ni_2In_4$ at 20 K; small green (light blue) balls represent the Ni (In) atoms. (b) Observed (dots, red), calculated (line, black) and difference pattern of the (2 K–130 K) data of $Tb_5Ni_2In_4$. The tick marks indicate the calculated position of the magnetic Bragg peaks for $\kappa_1 = (0, 0, 0)$ (first row) and of $\kappa_2 = (0, 0.636, ½)$ (second row).

Table 3. Basis vectors (BV) of the allowed irreducible representations (IR) for $\kappa = (0, \delta, ½)$ for Wyckoff positions 2*a* and 4*g* (splits into two orbits); *R* = real, *I* = imaginary component, $\alpha = -\cos(\pi\delta)$, $\beta = \sin(\pi\delta)$. Refined values of the coefficients of the BV's of the incommensurate cycloidal spiral structure and total maximum magnetic moment values μ_{Tb} for $Tb_5Ni_2In_4$ at 2 K resulting from the superposition of the $\kappa = (0, 0, 0)$ (see table 2) and the $\kappa = (0, \delta, ½)$ components.

			IR1	IR2		IR3	IR4		
$\kappa = (0, \delta, ½)$			BV1	BV1	BV2	BV1	BV1	BV2	
x, *y*, *z*		R	0 0 1	1 0 0	0 1 0	0 0 1	1 0 0	0 1 0	
		I	0 0 0	0 0 0	0 0 0	0 0 0	0 0 0	0 0 0	
$-x + ½, y + ½, -z$		R	$0\ 0\ \alpha$	$\alpha\ 0\ 0$	$0\ -\alpha\ 0$	$0\ 0\ -\alpha$	$-\alpha\ 0\ 0$	$0\ \alpha\ 0$	
		I	$0\ 0\ \beta$	$\beta\ 0\ 0$	$0\ -\beta\ 0$	$0\ 0\ -\beta$	$-\beta\ 0\ 0$	$0\ \beta\ 0$	
	ϕ(°/2π)								μ_{Tb} [μ_B]
Tb1	–0.44(1)			−1.4(2)	2.9(2)				8.5(1)
Tb2_1	0			2.7(3)	−6.7(2)				6.7(2)
Tb2_2	–0.16(1)			2.7(3)	−6.7(2)				6.7(2)
Tb3_1	0.37(1)			−1.4(2)	−2.9(2)				8.5(1)
Tb3_2	–0.25(1)			−1.4(2)	−2.9(2)				8.5(1)

The new magnetic Bragg peaks appearing below $T_N = 20$ K can be indexed with the incommensurate magnetic propagation vector $\kappa_2 = (0, 0.636, ½)$. Unlike in $Ho_5Ni_2In_4$, this new magnetic order does not replace the ferromagnetic one found above 20 K but it adds itself to the existing one. Table 3 displays the results of magnetic symmetry analysis for $\kappa_2 = (0, \delta, ½)$ for the Wyckoff sites 2*a* (Tb1) and 4*g* (Tb2, Tb3). Under the action of the magnetic propagation vector the 4-fold site on 4*g* gets split into two independent orbits leading to five (in theory independent) Tb sites, which all possess the same allowed IR's.

Testing the different IR's it became clear that only IR2 is able to account for the measured intensities and that most of the magnetic scattering of this low temperature incommensurate magnetic structure originates from the Tb2 sublattice which stays non-magnetic above 20 K. The arrangement represents a cycloidal spiral [25], running along the *b*-direction with moments circulating within the (0 0 1) plane. The relatively small contributions from the Tb1 and the two Tb3 sublattices to this incommensurate modulation were found to be similar and therefore fixed in the final refinement to equal absolute values for both BV's. As usual for incommensurate magnetic structures, phases relating the different sublattices relative to each other were refined. The refined values for the different BV's and the resulting total magnetic moment values are listed in table 3 ($R_{\mathrm{Mag}} = 10.4$ for the cycloidal spiral phase); Figure 12(b) displays the refinement of the 2 K–130 K difference data. Using the model of a canted longitudinal sine wave for the refinement of the incommensurate magnetic phase worsens the refinement ($R_{\mathrm{Mag}} = 11.8$). We have to recall here that both magnetic propagation vectors are acting through the whole sample volume; $\kappa_1 = (0, 0, 0)$ only on the Tb1 and Tb3 sublattices and $\kappa_2 = (0, 0.635, ½)$ mostly on the Tb2 sublattice. Figure 13(a) separately displays the incommensurate magnetic arrangement, while figure 13(b) shows the magnetic structure resulting from the superposition of the two magnetic contributions.

The total maximum magnetic moment values at 2 K (table 3) amount to 8.5 μ_{B} for Tb1 and Tb3, only slightly less than the expected magnetic moment for the Tb^{3+} ion of 9.0 μ_{B}. For the Tb2-sublattice, which orders magnetically only below 20 K, we infer a value of 6.8 μ_{B}. Trying to refine the magnetic scattering at 2 K restricting the incommensurate contribution to only the Tb2-sublattice worsens the fit noticeably. The appearance of small incommensurate components as well on the Tb1- and the Tb3-sublattices goes in line with the slight reduction of the ferromagnetic component on these sites when cooling from 20 K down to 2 K (table 2).

3.2.3. $Tb_{11}Ni_4In_9$. High resolution data taken at $T = 300$ K confirm the $\mathrm{Nd_{11}Pd_4In_9}$ prototype (with space group *Cmmm*) for $\mathrm{Tb_{11}Ni_4In_9}$ and the phase purity of the sample. The crystallographic details are given in table 4. There is no change of the crystallographic structure down to 2 K. Figure 14 shows the thermodiffractogram of the compound between 2 K and 150 K.

Table 4. Results of Rietveld refinement of the high resolution neutron diffraction data of $R_{11}\mathrm{Ni_4In_9}$ (R = Tb, Ho) at $T = 300$ K, *R*5 on Wyckoff site 2*a*, In3 on 2*c*.

R		Tb	Ho
*R*1 (8*p*)	*x*	0.2432(3)	0.2436(3)
	y	0.1698(2)	0.1691(2)
*R*2 (4*i*)	*y*	0.1600(3)	0.1591(3)
*R*3 (4*i*)	*y*	0.3733(3)	0.3730(3)
*R*4 (4*g*)	*x*	0.3106 (4)	0.3110(4)
*R*5 (2*a*)			
Ni (8*q*)	*x*	0.3476(2)	0.3482(3)
	y	0.1021(2)	0.1015(2)
In1 (8*q*)	*x*	0.1041(4)	0.1048(5)
	y	0.2612(4)	0.2609(5)
In2 (8*q*)	*x*	0.1437(6)	0.1432(7)
	y	0.0702(4)	0.0702(5)
In3 (2*c*)			
a		14.4007(6)	14.2898(7)
b		21.6316(9)	21.4764(10)
c		3.6294(1)	3.6023(2)
R_{Bragg}		8.3	7.3

Large changes in the Bragg peak intensities and the appearance of new Bragg peaks are clearly visible upon lowering the temperature. The inset shows details of the low angle region in a contour plot where weaker intensities have been enhanced by using logarithmic scale. Three transition temperatures can be discerned; the integration of characteristic peaks allows to determine the transition temperatures as $T_{\mathrm{C1}} = 115$ K, $T_{\mathrm{N2}} = 35$ K and $T_{\mathrm{N3}} = 20$ K. These values are in a good agreement with those obtained from macroscopic measurements [5, 7]. Magnetic peaks in the temperature region between 115 K and 35 K can be indexed with the magnetic propagation vector $\kappa_1 = (0, 0, 0)$. Table 5 lists the allowed IR's and their BV's for this propagation vector in the space group *Cmmm* for the Wyckoff sites 8*p* (Tb1), 4*i* (Tb2, Tb3), 4*g* (Tb4) and 2*a* (Tb5).

Data taken just above T_{N2}, at $T = 35$ K, were refined testing the different allowed IR's. Only IR3 is able to describe correctly the measured magnetic peak intensities. IR3 represents a simple ferromagnetic arrangement with spins pointing in the *c*-direction; table 5 lists the refined magnetic moment values. Only three out of five Tb-sublattices participate in this order: whereas the magnetic moments on the Tb2- and the Tb5-sublattices, of about 8 μ_{B}, are already close to the Tb^{3+} free ion moment of 9 μ_{B}, the Tb1-sublattice sees only a reduced magnetic moment of about 4 μ_{B} with the other two sublattices remaining non-ordered. Within each of these sublattices the Tb-spins are ferromagnetically aligned to each other; however, while the Tb1- and Tb2-sublattices point in the same direction, the Tb5-sublattice is ferrimagnetically aligned to them. Figure 15(a) displays this magnetic structure. The cyclic refinement of the high intensity data between 35 K and T_{C} (figure 15(b)) reveals a strongly differing temperature dependence of the three sublattices. Just 15 K below $\mathrm{T_C}$ the magnetic moment of the Tb2-sublattice has already attained nearly 70% of its value at 35 K, while the corresponding figures for the Tb1- and the Tb5-sublattice are much lower, with values at 50% and 30%, respectively. In particular, the weak and nearly linear temperature dependence of the Tb5-sublattice moment points to its induced character. A change of slope at about 80 K indicates that below this temperature the increase of the magnetic moment on the Tb5-sublattice is supported by an additional magnetic interaction.

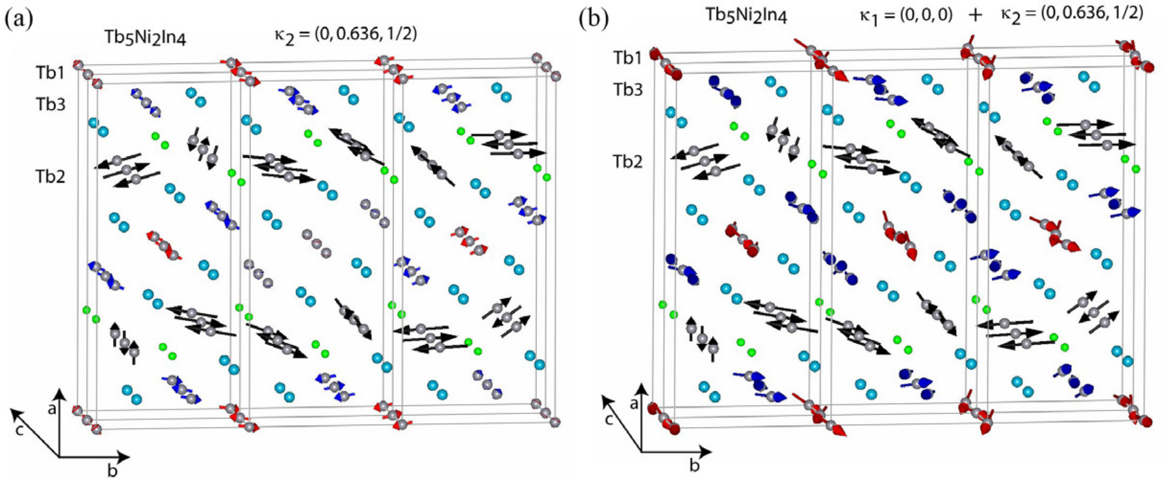

Figure 13. (a) Incommensurate magnetic arrangement in $Tb_5Ni_2In_4$ at 2 K; small green (light blue) balls represent the Ni (In) atoms. (b) Magnetic structure of $Tb_5Ni_2In_4$ at 2 K resulting from the superposition of the commensurate and the incommensurate magnetic structures.

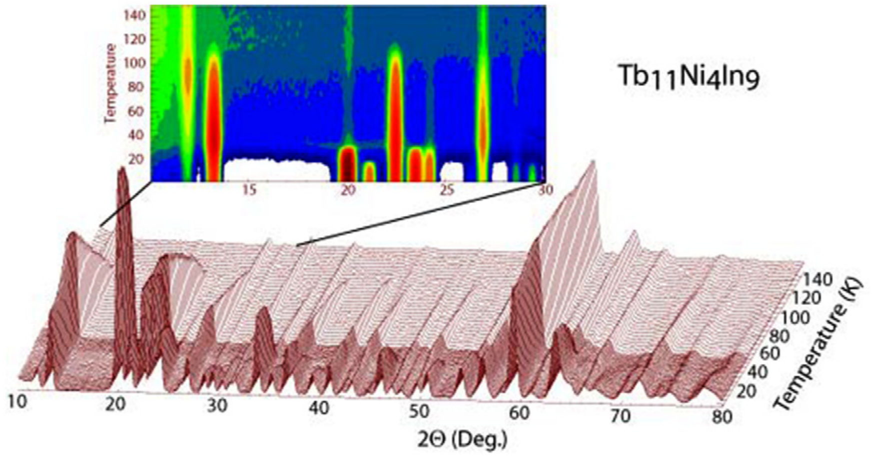

Figure 14. Thermodiffractogram of $Tb_{11}Ni_4In_9$ between 2 K and 150 K. The inset represents a contour plot of the low angle part of the thermodiffractogram where the intensity contours follow a logarithmic scale.

Magnetic peaks appearing below $T_{N2} = 35$ K can be indexed with the magnetic propagation vector $\kappa_2 = (0, 0, ½)$; magnetic symmetry analysis shows that for this propagation vector the IR's and their BV's are identical to those of $\kappa_1 = (0, 0, 0)$ listed in table 5. Figure 14 shows that both sets of magnetic peaks are coexisting. Those formed below $T_{C1} = 115$ K are only changing slightly in intensity (a change largely attributed to a reduction of the paramagnetic background scattering) pointing to a situation where either different parts of the sample volume follow different magnetic propagation vectors or where both propagation vectors are superimposed in the complete sample volume. Data taken at $T = 21$ K, e.g. just above $T_{N3} = 20$ K, were refined testing the different IR's and their BV's; they show that the new magnetic ordering follows BV1 of IR7 and BV2 of IR5. These BV's describe a simple ferromagnetic arrangement between spins of one sublattice within the original chemical unit cell, with components in the *a*- and *b*-directions. An antiferromagnetic order in the *c*-direction is then described by the magnetic propagation vector $\kappa_2 = (0, 0, ½)$. Table 5 lists the refined coefficients, while figure 15(a) displays this magnetic structure. Table 5 lists as well the refined values at $T = 21$ K for the persisting $\kappa_1 = (0, 0, 0)$ magnetic order.

The fact that the magnetic moment of the Tb3-sublattice [which has no contribution from the $\kappa_1 = (0, 0, 0)$ ordering] amounts to $\mu_{Tb3} = 9.3(7)\ \mu_B$, together with the still large moments of about 8 μ_B on the Tb2- and Tb5- sublattices within the $\kappa_1 = (0, 0, 0)$ ordering, indicates that both magnetic arrangements must involve the whole sample volume as otherwise the refined moment values would become too large. Assuming that e.g. 50% of the volume sample sees the first magnetic order and the other 50% the second magnetic order, all refined moment values would be $\sqrt{2}$ times larger and therefore largely above the theoretical limit for the free ion Tb^{3+} of $\mu_{Tb3+} = 9\ \mu_B$.

Looking at the refined magnetic moment values in table 5 and at figure 16(a), one can realize that the second magnetic transition is primarily associated with the ordering of the Tb3-sublattice while the Tb4-sublattice still does not order magnetically. Significant contributions from the κ_2 ordering are as well present on the Tb1- and the Tb5-sublattices: the Tb2-sublattice, which had been the first to order spontaneously at

Table 5. Basis vectors (BV) of the allowed irreducible representations (IR) for $\kappa = (0, 0, 0), (0, 0, ½), (0, 1, ½)$ and $(0, 1, 0)$ for Wyckoff positions 8*p*, 4*i*, 4*g* and 2*a* of the space group *Cmmm*; refined values of the coefficients of the BV's and total magnetic moment values for $Tb_{11}Ni_4In_9$ at 35 K, 21 K and 2 K.

	IR1	IR2		IR3	IR4		IR5		IR6	IR7		IR8		
	BV1	BV1	BV2	BV1	BV1	BV2	BV1	BV2	BV1	BV1	BV2	BV1		R_{Mag}
R (8*p*) *x*, *y*, *z*	0 0 1	1 0 0	0 1 0	0 0 1	1 0 0	0 1 0	1 0 0	0 1 0	0 0 1	1 0 0	0 1 0	0 0 1		
−*x*,−*y*, *z*	0 0 1	−1 0 0	0 −1 0	0 0 1	−1 0 0	0 −1 0	1 0 0	0 1 0	0 0 −1	1 0 0	0 1 0	0 0 −1		
−*x*, *y*, −*z*	0 0 −1	−1 0 0	0 1 0	0 0 1	1 0 0	0 −1 0	−1 0 0	0 1 0	0 0 −1	1 0 0	0 −1 0	0 0 1		
x,−*y*, −*z*	0 0 −1	1 0 0	0 −1 0	0 0 1	−1 0 0	0 1 0	−1 0 0	0 1 0	0 0 1	1 0 0	0 −1 0	0 0 −1		
R (4*i*) *x*, *y*, *z*			0 1 0	0 0 1	1 0 0			0 1 0		1 0 0		0 0 1		
−*x*, −*y*, *z*			0 −1 0	0 0 1	−1 0 0			0 1 0		1 0 0		0 0 −1		
R (4*g*) *x*, *y*, *z*		1 0 0		0 0 1		0 1 0		0 1 0	0 0 1	1 0 0				
−*x*, −*y*, *z*		−1 0 0		0 0 1		0 −1 0		0 1 0	0 0 −1	1 0 0				
R (2*a*) *x*, *y*, *z*				0 0 1				0 1 0		1 0 0				
$T = 35$ K				$\kappa_1 = (0, 0, 0)$									μ_{Tb} [μ_B]	5.9
Tb1				3.8(2)									3.8(2)	
Tb2				8.1(3)									8.1(3)	
Tb3				0									0	
Tb4				0									0	
Tb5				−8.2(4)									8.2(4)	
$T = 21$ K				$\kappa_1 = (0, 0, 0)$					$\kappa_2 = (0, 0, ½)$					4.8, 6.7
Tb1				3.1(3)				0		6.0(3)			6.7(3)	
Tb2				8.2(4)				−3.1(7)		1.5 (5)			8.9(7)	
Tb3				0				3.6(8)		8.6(5)			9.3(8)	
Tb4				0				0		0			0	
Tb5				−8.1(5)				−6.4(8)		0			10.3(9)	
$T = 2$ K				$\kappa_1 = (0, 0, 0)$					$\kappa_2 = (0, 0, ½)$					5.2, 6.1, 10.2
									or $\kappa_3 = (0, 1, ½)$ for Tb4					
Tb1				2.2(3)				0		6.8(5)			7.1(5)	
Tb2				8.6(5)				−4.0(7)		1.6(6)			9.6(9)	
Tb3				0				3.8(8)		9.2(5)			9.9(8)	
Tb4				0				8.9(3)		0			8.9(3)	
Tb5				−7.6(5)				−6.8(8)		0			10.2(9)	

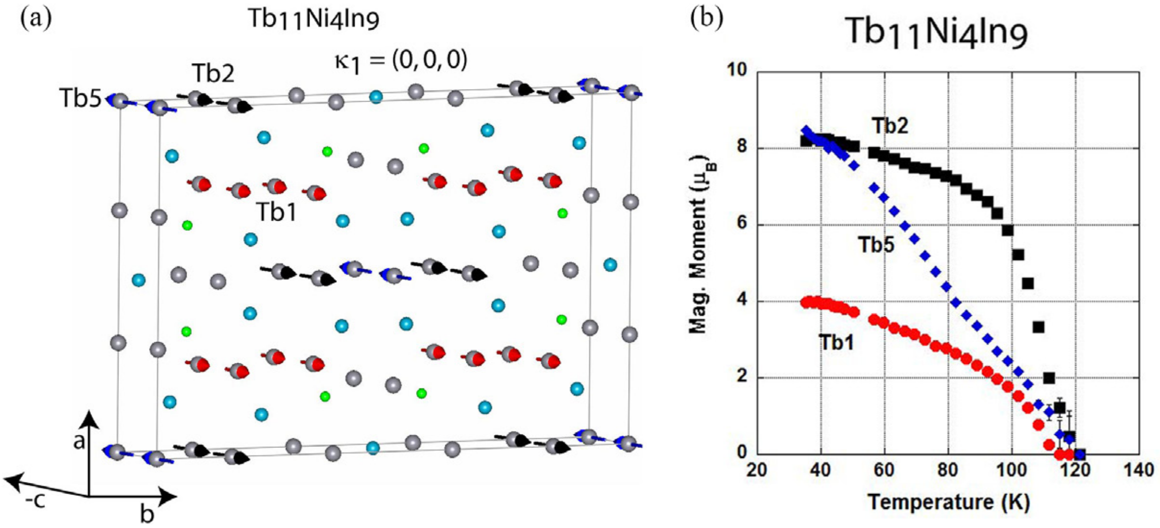

Figure 15. (a) Magnetic structure of $Tb_{11}Ni_4In_9$ between $T_{C1} = 115$ K and $T_{N2} = 35$ K; small green (light blue) balls represent the Ni (In) atoms. (b) Thermal dependence of the magnetic moments on the Tb1-, Tb2- and Tb5-sublattices.

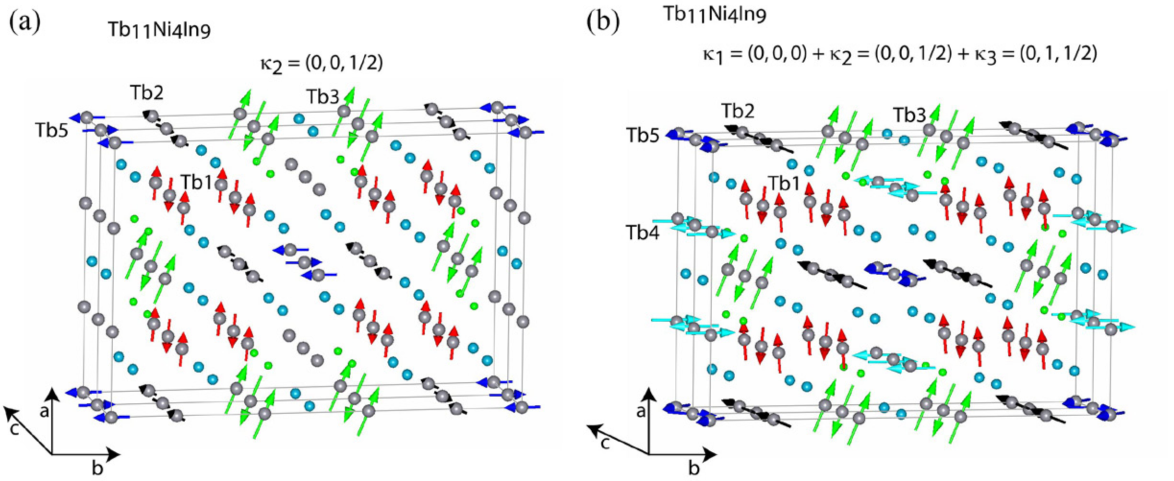

Figure 16. (a) Additional magnetic order with $\kappa_2 = (0, 0, ½)$ in $Tb_{11}Ni_4In_9$ appearing below $T_{N2} = 35$ K; small green (light blue) balls represent the Ni (In) atoms. (b) Magnetic structure at 2 K.

T_{C1} (figure 15(b)), sees only a small additional magnetic contribution through κ_2.

The lowest magnetic transition of $Tb_{11}Ni_4In_9$ at $T_{N3} = 20$ K creates additional magnetic reflections which are indexed with the magnetic propagation vector $\kappa_3 = (0, 1, ½)$. It reflects the appearance of magnetic order on the Tb4-sublattice; $\mu_{Tb4} = 8.9(3)$ μ_B at 2 K (table 5). Following BV2 of IR5, this order sees the magnetic spins on Tb4 sites, which are connected through the C-centering operation, aligned antiparallel and oriented solely in *b*-direction. A doubling of the chemical unit cell through the antiferromagnetic sequence along the *c*-axis is created through this $\kappa_3 = (0, 1, ½)$ ordering, as in the case of the second magnetic order where $\kappa_2 = (0, 0, ½)$. Figure 16(b) displays the magnetic structure adopted by $Tb_{11}Ni_4In_9$ at the lowest temperature with the three magnetic propagation vectors acting on the same sample volume. A plot of the refinement of the neutron data taken at 2 K is shown in figure 17. The magnetic moment values are slightly higher compared to the free ion moment of 9 μ_B for Tb^{3+} in the Tb3- and Tb5-sublattices; we attribute this result more to the uncertainties of the multiphase refinement rather than to a possible contribution of the conduction electrons.

3.2.4. $Ho_{11}Ni_4In_9$. High resolution data taken at $T = 300$ K confirm the crystal structure of $Ho_{11}Ni_4In_9$ and the phase purity of the sample. The crystallographic details are reported in table 4. Data taken at low temperature confirm the absence of any structural phase transition. Similar to the Tb-compound $Ho_{11}Ni_4In_9$ undergoes several magnetic transitions on cooling down. Figure 18 shows the thermodiffractogram in the form of a contour plot: at least five different temperature regions can be discerned.

Magnetic Bragg peaks appearing at the first transition temperature of about $T_{N1} = 22$ K have to be divided into those that disappear at about 9 K ($2\Theta = 3.9°, 9.2°, 14.9°, 18.9°$) and those which persist down to the lowest temperature ($2\Theta = 6.6°, 16.9°, 34°, 41.9°$). These two sets can respectively be indexed with the magnetic propagation vectors

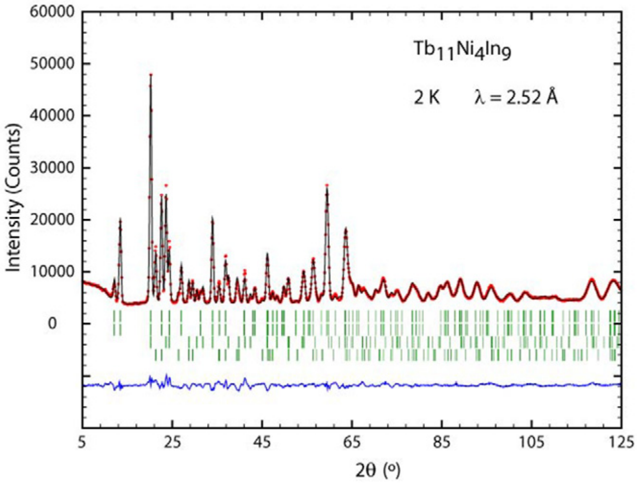

Figure 17. Observed (dots, red), calculated (line, black) and difference pattern of the 2 K data of $Tb_{11}Ni_4In_9$. The tick marks indicate the calculated position of the nuclear Bragg peaks (first row) and of the magnetic peaks for $\kappa_1 = (0, 0, 0)$ (second row), $\kappa_2 = (0, 0, ½)$ (third row) and $\kappa_3 = (0, 1, ½)$ (fourth row).

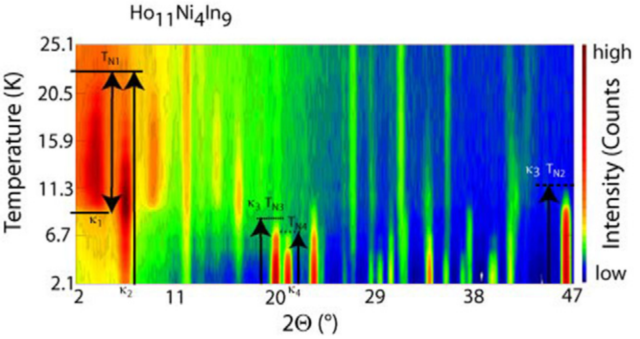

Figure 18. Thermodiffractogram of $Ho_{11}Ni_4In_9$ between 2 K and 25 K. The temperatures T_{N1}–T_{N4}, where changes in the magnetic structures appear and the temperatures regions of existence for the different magnetic propagation vectors, are indicated. For details see the main text.

$\kappa_1 = (0, 0.62, 0)$ and $\kappa_2 = (0, 1, 0)$. A second transition occurs at about $T_{N2} = 12$ K creating magnetic peaks at $2\Theta = 23.7°$, 37.8°, 46.5° and 64.1°, which can be indexed with a third magnetic propagation vector $\kappa_3 = (0, 0, ½)$. At $T_{N3} = 8$ K there is a further change in the spectrum with additional peaks appearing at $2\Theta = 20.2°$, 34.2° and 41.5° which are again indexed with $\kappa_3 = (0, 0, ½)$. Finally, yet another magnetic transition takes place at $T_{N4} = 7$ K with new Bragg peaks at $2\Theta = 21.4°$, 28.9°, 29.7°, 35.6° and 39.8° which is characterized by a fourth magnetic propagation vector $\kappa_4 = (0, 1, ½)$. Table 6 lists the IR's and their BV's allowed for $\kappa_1 = (0, \delta, 0)$ in the *Cmmm* space group for the five different Wyckoff sites occupied by Ho. Under the action of this incommensurate propagation vector the 8*p* and the two 4*i* sites get each split into two different orbits creating thereby eight independent Ho sites.

The large number of possible independent parameters would normally make a refinement of the magnetic structure determined by this propagation vector very difficult; however, it turns out that only one of the Ho-sublattices, namely the Ho2 site, follows this magnetic ordering. For the commensurate magnetic propagation vectors $\kappa_2 = (0, 1, 0)$, $\kappa_3 = (0, 0, ½)$ and $\kappa_4 = (0, 1, ½)$ the IR's and their BV's are listed in table 5. As explained above there is a coexistence of solely $\kappa_1 = (0, 0.62, 0)$ and $\kappa_2 = (0, 1, 0)$ within the temperature range $22\,K < T \leqslant 12\,K$. Testing different proposed solutions it is found that within this temperature region the magnetic structure can be described by the Ho2-sublattice following BV1 of IR4 (table 6) with $\kappa_1 = (0, 0.62, 0)$, and the Ho5-sublattice following BV1 of IR7 (table 5) with $\kappa_2 = (0, 1, 0)$.

Table 6. Basis vectors (BV) of the allowed irreducible representations (IR) for $\kappa = (0, \delta, 0)$ for Wyckoff positions 8*p*, 4*i*, 4 *g* and 2*a* of space group *Cmmm*.

	IR1	IR2		IR3	IR4	
$\kappa = (0, \delta, 0)$	BV1	BV1	BV2	BV1	BV1	BV2
R (8*p*, 4*g*) *x*, *y*, *z*	0 0 1	1 0 0	0 1 0	0 0 1	1 0 0	0 1 0
−*x*, *y*,−*z*	0 0 −1	−1 0 0	0 1 0	0 0 1	1 0 0	0 −1 0
R (4*i*, 2*a*) *x*, *y*, *z*			0 1 0	0 0 1		1 0 0

Both BV's correspond to spins pointing in direction of the *a*-axis, with the magnetic moment on the Ho2 site being sinusoidally modulated in the *b*-direction. Figure 19(a) shows the refinement of the data taken at 16 K; figure 19(b) depicts a picture of the resulting magnetic structure. The magnetic moment value of the Ho5 site at $T = 16$ K amounts to $\mu_{Ho5} = 5.3(2)\ \mu_B$, while the amplitude on the Ho2 site has a maximum value of $\mu_{Ho2} = 7.8(2)\ \mu_B$. On lowering the temperature down to 12 K, an increase of μ_{Ho5} to 6.8(3) μ_B is seen and small extra magnetic contributions (1–2 μ_B) appear within this $\kappa_2 = (0, 1, 0)$ order on the Ho1-, Ho2- and Ho4-sublattices. The Ho3-sublattice stays magnetically non-ordered. The magnetic arrangement following $\kappa_1 = (0, 0.62, 0)$ remains restricted to the Ho2-sublattice and reaches its maximum amplitude at 12 K with $\mu_{Ho2} = 9.4(2)\ \mu_B$. The value δ of this incommensurate propagation vector of type $\kappa = (0, \delta, 0)$ does not show any variation with temperature. Below 12 K the κ_1 magnetic order decreases rapidly and disappears at 9 K; at the same time, the $\kappa_2 = (0, 1, 0)$ magnetic ordering goes through a maximum at about 10 K before decreasing as well with the increase of the $\kappa_3 = (0, 0, ½)$ structure. Table 7 gives in detail the individual components for the different Ho-sublattices as a function of temperature.

Below $T_{N2} = 12$ K the new magnetic pattern characterized by $\kappa_3 = (0, 0, ½)$ affects first only the Ho1-, Ho2- and Ho5-sublattices. Following IR3 (table 5) the spins are oriented along the *c*-direction; the magnetic propagation vector leads to a doubling of the unit cell in the *c*-direction. This magnetic transition seems to be strongly influenced by the application of a modest external magnetic field as indicated by the heat capacity data presented in section 3.1.4 (see figure 5(b)) and by the presence of a metamagnetic transition (see figure 6(b)). The peak at about 10.5 K in the heat capacity data (measured on heating) should be associated to the appearance of the incommensurate $\kappa_1 = (0, 0.62, 0)$ antiferromagnetic structure. Its disappearance under a magnetic field indicates a suppression of this magnetic transition and probably the persistence of the

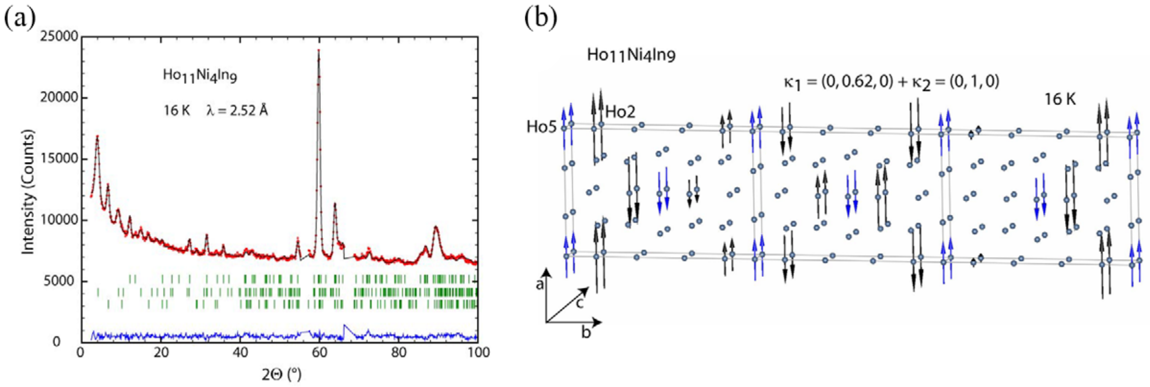

Figure 19. (a) Observed (dots, red), calculated (line, black) and difference pattern of the 16 K data of $Ho_{11}Ni_4In_9$. The tick marks indicate the calculated position of the nuclear Bragg peaks (first row) and of the magnetic peaks for $\kappa_1 = (0, 0.62, 0)$ (second row), $\kappa_2 = (0, 1, 0)$ (third row). Two regions of the spectrum, where aluminum peaks of the cryostat appeared, were excluded from the refinement. (b) Magnetic structure of $Ho_{11}Ni_4In_9$ between $T_{N1} = 22$ K and $T_{N2} = 12$ K.

$\kappa_3 = (0, 0, ½)$ type magnetic structure. At 9 K this ordering with $\kappa_3 = (0, 0, ½)$ has completely replaced the $\kappa_1 = (0, 0.62, 0)$ order of the Ho2-sublattice and at 8 K it becomes dominant for the Ho1- and Ho5-sublattices (table 7) compared to the κ_2 phase. At this lower temperature the transition visible in the thermodiffractogram (figure 18), and labeled $T_{N3} = 8$ K, is linked to the first appearance of a magnetic moment on the Ho3-sublattice. Following BV1 of IR7 the Ho3 spins are oriented along the *a*-axis with a magnetic moment value which increases steadily up to $\mu_{Ho3} = 9.3(2)\ \mu_B$ as the temperature is lowered to 2 K (table 7). At the lowest magnetic transition $T_{N4} = 7$ K the Ho4-sublattice finally becomes magnetically ordered with $\kappa_4 = (0, 1, ½)$ following BV2 of IR5. The spins of the Ho4 sites are oriented along the *b*-direction with a doubling of the unit cell in the *c*-direction; spins connected through the C-centering are antiparallel. At the base temperature of $T = 2$ K the magnetic moment value amounts to $\mu_{Ho4} = 8.9(2)$ μ_B. Contrary to the Ho3-sublattice (κ_3) and the Ho4-sublattice (κ_4), which are each only characterized by one type of magnetic order, the other three Ho-sublattices see a superposition of two magnetic arrangements (κ_2 and κ_3). Table 7 shows that, however, at 2 K the κ_3 order is largely dominant for the Ho2- and the Ho5-sublattices. Calculating total magnetic moment values resulting from the two magnetic contributions one gets values of $\mu_{Ho2} = 6.6(2)\ \mu_B$ and $\mu_{Ho5} = 7.6(2)\ \mu_B$. As the Ho1-sublattice is following the same BV1 of IR7, with the two different magnetic propagation vectors $\kappa_2 = (0, 1, 0)$ and $\kappa_3 = (0, 0, ½)$, there exist two different Ho1 sites with two different total magnetic moments: $\mu_{Ho1} = 5.0(0)$ or $6.0(3)\ \mu_B$. In view of the different thermal dependence of the κ_2 and the κ_3 structure, the first starting to decline below 10 K and the second increasing at the same time, it is possible to envisage that these orders are not acting on the same sample volume but that a separation into different parts of the volume is present. This would mean that at $T = 2$ K a small part of the sample volume sees exclusively the κ_2 magnetic arrangement while the majority part sees the κ_3 ordering for the Ho1, Ho2, Ho3 and Ho5 sites and the κ_4 order for the Ho4 site. It is not possible to decide from the neutron data which scenario is the true one; it is only possible to say that a phase separation into 10% κ_2 phase and 90% κ_3/κ_4 phase would result within each phase in maximum magnetic moment values not too large compared to the free ion value of $\mu_{Ho3+} = 10\ \mu_B$.

3.2.5. Discussion of the magnetic structures. The fibrous microstructure of the $R_{11}Ni_4In_9$ compounds is characterized by the existence of rods built up by '$R_8Ni_4In_9$' units which run along the *c*-direction [4]. The *R*3 and the *R*4 atomic positions are within these rods, the *R*1 position is at the edges of the rods, and the *R*2 and *R*5 positions are outside and between the rods. The 'Ni_4' framework has close contact distances to rare earth atoms on the *R*1-, *R*3- and *R*4-sublattices ($d_{R-Ni} \approx 2.8 - 2.9$ Å), while the distances to *R*2 and *R*5 positions are very large ($d_{R-Ni} > 5$ Å). This special structural unit seems to have a strong influence on the temperature dependent development of long range magnetic order on the different rare earth sublattices of the compounds. Both $Ho_{11}Ni_4In_9$ (figure 21(a)) and $Tb_{11}Ni_4In_9$ (figure 21(b)) experience first the magnetic ordering of the *R*2 and the *R*5 positions; however, the Ho5 ordering is less developed than the ordering of the Ho2 site at equivalent temperatures (table 7, see values at 16 K and 12 K), while the Tb5 ordering is apparently induced by the Tb2-sublattice (figure 15(b)). The moment value of the Tb1-sublattice is significantly reduced compared to those of the Tb2 and Tb5 sublattices below T_{C1} (figure 15(b)), while in $Ho_{11}Ni_4In_9$ the Ho1 sublattice orders at a distinctively lower temperature (12 K, see table 7).

Next to order are the *R*3-sublattices, while in both compounds the *R*4-sublattices are only ordered at the lowest temperatures. We are not aware of any other intermetallic compound where a similar separate magnetic ordering of numerous rare earth sublattices is found. Assuming that the establishment of magnetic order is linked to the existence of a network of $R - R$ interactions, it is found that the nearest R-R neighbors for both the *R*3- and the *R*4-sublattices belong to the same sublattice (at a distance corresponding to the *c*-lattice parameter of ≈3.6 Å), while the distances to the *R*1-sublattice and to the respective other sublattice ($R3 - R4$) are substantially longer (≈3.8 Å). There is no close contact between sublattices *R*1, *R*3 and *R*4 with the *R*2- and *R*5-sublattices. The

Table 7. Refined values of the coefficients (μ_B) of the BV's for the four different magnetic phases in $Ho_{11}Ni_4In_9$ [characterized respectively by $\kappa_1 = (0, \delta, 0)$, $\kappa_2 = (0, 1, 0)$, $\kappa_3 = (0, 0, ½)$ and $\kappa_4 = (0, 1, ½)$] as a function of temperature for the five different Ho-sublattices. R_{Mag} values are given separately for each magnetic phase.

		κ_1	κ_2		κ_3	R_{Mag}		
			BV1	BV2				
T[K]		BV1 (IR4)		(IR7)	BV1 (IR3)	K_1	K_2	K_3
16						6.4	16.2	
	Ho1							
	Ho2	7.8(2)						
	Ho3							
	Ho4							
	Ho5		5.3(2)					
12						3.7	9.9	
	Ho1		0.6(2)	1.7(2)				
	Ho2	9.4(2)	1.0(2)	—				
	Ho3		—	—				
	Ho4		0.9(2)	—				
	Ho5		6.8(3)	—				
10						5.4	7.6	9.3
	Ho1		0.9(2)	1.6(2)	2.4(2)			
	Ho2	6.7(2)	0.8(2)	—	3.3(3)			
	Ho3		—	—	—			
	Ho4		1.2(2)	—	—			
	Ho5		7.2(3)	—	2.1(4)			
9							10.1	7.4
	Ho1		1.7(2)	2.4(2)	3.5(2)			
	Ho2	0	2.3(3)	—	5.6(2)			
	Ho3		—	—	—			
	Ho4		—	—	—			
	Ho5		6.3(4) -		5.0(2)			

		κ_2		κ_3		κ_4	R_{Mag}		
T[K]		BV1 (IR7)	BV2	BV1 (IR7)	BV1 (IR3)	BV2 (IR5)	κ_2	κ_3	κ_4
8							7.9	6.4	
	Ho1	1.5(2)	2.3(2)	—	4.0(2)				
	Ho2	2.1(3)	—	—	6.1(2)				
	Ho3	—	—	2.1(3)	—				
	Ho4	—	—	—	—				
	Ho5	5.1(3)	—	—	5.7(2)				
7							7.4	6.0	
	Ho1	1.9(2)	2.6(2)	—	4.3(2)				
	Ho2	2.3(2)	—	6.3(2)	—				
	Ho3	—	—	3.2(2)	—				
	Ho4	—	—	—	—				
	Ho5	3.0(3)	—	—	6.2(2)				
6							6.5	5.9	10.1
	Ho1	1.6(2)	2.6(2)	1.3(2)	4.2(2)	—			
	Ho2	2.4(3)	—	6.4(2)	—	—			
	Ho3	—	—	5.7(2)	—	—			
	Ho4	—	—	—	—	4.1(2)			
	Ho5	2.6(3)	—	6.7(2)	—	—			
2							7.9	5.2	5.9
	Ho1	1.2(2)	2.4(2)	2.4(2)	4.2(2)	—			
	Ho2	2.1(4)	—	6.2(2)	—	—			
	Ho3	—	—	9.3(2)	—	—			
	Ho4	—	—	—	—	8.9(2)			
	Ho5	1.7(4)	—	—	7.3(2)	—			

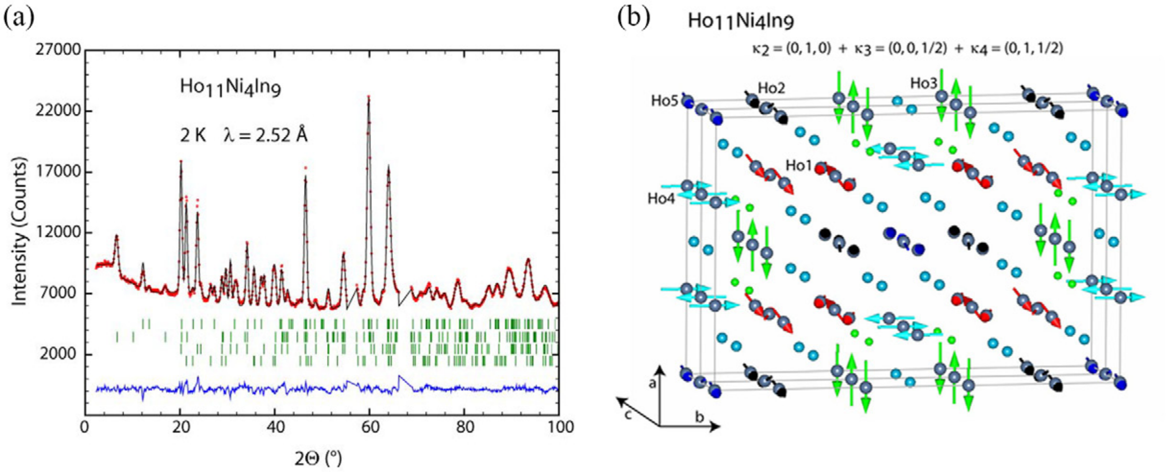

Figure 20. (a) Observed (dots, red), calculated (line, black) and difference pattern of the 2 K data of $Ho_{11}Ni_4In_9$. The tick marks indicate the calculated position of the nuclear Bragg peaks (first row) and of the magnetic peaks for $\kappa_2 = (0, 1, 0)$ (second row), $\kappa_3 = (0, 0, ½)$ (third row) and $\kappa_4 = (0, 1, ½)$. (b) Magnetic structure of $Ho_{11}Ni_4In_9$ at 2 K; small green (light blue) balls represent the Ni (In) atoms.

closest distance between *R*-sublattices is found between the *R*2- and *R*5-sublattices (≈3.4 Å for R = Ho at 300 K). A 3D network is formed by the *R*2-, *R*5- and *R*1-sublattices, as the $R1 - R2$ and $R1 - R1$ distances within the *a*-*b* plane are of the order of 3.5 Å. The existence of this network and of the generally closer $R - R$ distances could explain the hierarchical order in the temperature-dependent magnetic ordering of the sublattices detailed above. A strong hint for the importance of the inter-site distances in determining the appearance of magnetic order can be seen, as well, in the fact that in $Ho_{11}Ni_4In_9$ the magnetic propagation vector [$\kappa = (0, \delta, 0)$], determining the ordering of the Ho2 site which sets in at the highest temperature, is incommensurate within the *a*-*b* plane where the shortest inter-site distances are found.

Comparing the magnetic structures of the two $R_{11}Ni_4In_9$ compounds, one can make out several differences but ascertain strong similarities as well. While in the Tb-compound part of the magnetic order within *R*-sublattices (Tb2, Tb5 and Tb1) is of ferromagnetic nature resulting in a macroscopically detectable magnetic moment in zero fields, $Ho_{11}Ni_4In_9$ sees only antiferromagnetic interactions. Below the first magnetic transition the spins of the already magnetically ordered sublattices (Tb2, Tb5 and Tb1 for $T_{C1} > T > 35$ K, and Ho2 and Ho5 for $T_{N1} > T > 12$ K, respectively) point in the *c*-direction for the Tb-compound but they point in the *a*-direction for the Ho-compound. This reflects a strong influence of the rare earth single-ion anisotropy. The magnetic propagation vectors in these temperature regions are different with $\kappa = (0, 0, 0)$ for the Tb-compound and $\kappa = (0, \delta, 0)$ and (0, 1, 0) for $Ho_{11}Ni_4In_9$. While the strong magnetic order of the Tb2- and the Tb5- sublattices [following $\kappa = (0, 0, 0)$] persist down to the lowest temperatures, the magnetic interactions of the Ho2-sublattice [following $\kappa = (0, \delta, 0)$] disappear and those of the Ho5- sublattice [$\kappa = (0, 1, 0)$] strongly diminish when lowering the temperature. At lower temperatures both compounds see the development of magnetic interactions determined by the magnetic propagation vector $\kappa = (0, 0, ½)$ which comprise all the *R*-sublattices except the *R*4-sublattice. For both compounds the *R*3-sublattice follows exclusively this magnetic propagation vector, with spins oriented in the *a*-direction. A further strong similarity between the two $R_{11}Ni_4In_9$ compounds is the fact that in both cases the *R*4-sublattice is the last of the five sublattices to order and exclusively follows the magnetic propagation vector $\kappa = (0, 1, ½)$.

Strong similarities are found as well between the magnetic structures of the two $R_5Ni_2In_4$ compounds: both follow first the same magnetic propagation vector $\kappa = (0, 0, 0)$, and both seem to establish a further magnetic arrangement following an incommensurate magnetic propagation vector $\kappa = (0, \delta, ½)$ mostly involving the *R*2 site at the lowest temperatures. The magnetic order with $\kappa = (0, 0, 0)$ (IR3 and BV1 of IR7, see table 2) is ferromagnetic over the complete temperature range (below $T_C = 125$ K for Tb compound, and below $T_C = 25$ K for Ho compound), with spins oriented mainly in the *c*-direction. Similar to $R_{11}Ni_4In_9$ compounds it is possible to isolate in the $R_5Ni_2In_4$ structure a framework defined by the shortest Ni − In and In − In bonds. Figure 22 displays the rows of distorted pentagonal prisms RNi_4In_6 running along the *b*-axis which are superimposed in the *c*-direction. The *R*2 site is situated in the center of the polyhedron; *R*3 and *R*1 sites are positioned between the rows, with *R*1 being furthermore well isolated from the Ni sites. Again it is possible to establish a clear hierarchy by which the different rare earth sites get magnetically ordered with decreasing temperature. In both compounds $R_5Ni_2In_4$ (R = Ho and Tb) the *R*1 and the *R*3 sites are the first to order (table 2). In $Ho_5Ni_2In_4$, at 25 K, the *R*3 site possesses a magnetic moment value significantly lower than that of the Ho1. Figure 11 shows equally for $Tb_5Ni_2In_4$ that over a large temperature range the Tb3 site magnetic moment is lower than that of the Tb1 site and, furthermore, its magnetic moment seems to be induced by the magnetic order of the Tb1-sublattice. Magnetic ordering on the Tb2 site starts only below 20 K (compared to $T_C = 125$ K) and, moreover, follows a different magnetic propagation vector. In $Ho_5Ni_2In_4$ the Ho2 site possesses at 2 K a very small magnetic moment of about 1 μ_B and only below 2 K there are indications of a possible further magnetic ordering of this site following the same incommensurate magnetic propagation vector as

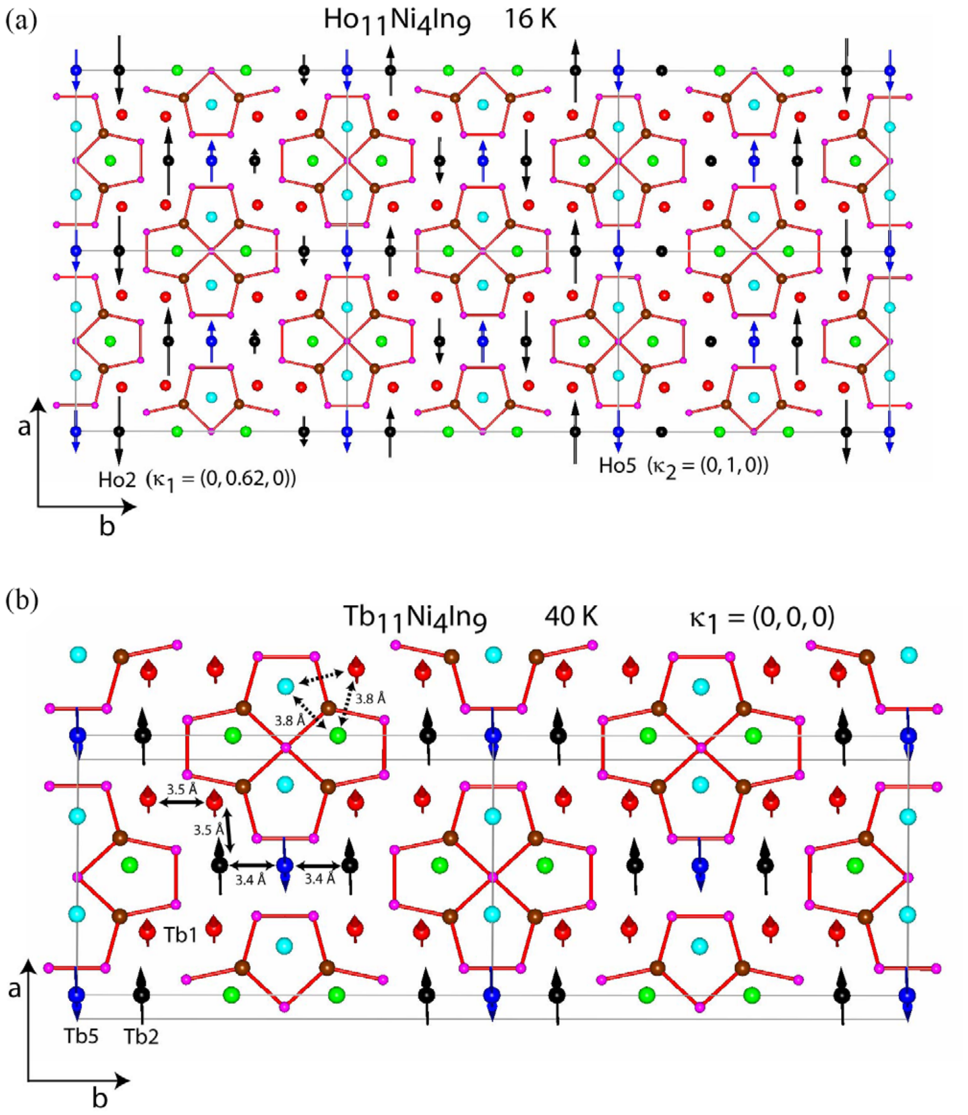

Figure 21. Position of the different R sites relative to the structural rod like element '$R_8Ni_4In_9$'; R1-5 (red, black, green, cyan, blue balls), Ni (brown balls), In (magenta balls), (a) Magnetic order in $Ho_{11}Ni_4In_9$ at 16 K developing only on the Ho2 and Ho5 sites situated in between the rods; view along the c-axis. (b) Magnetic order in $Tb_{11}Ni_4In_9$ at 40 K with non-magnetic Tb3 and Tb4 sites within the rods; view slightly inclined along the c-axis (moment direction). Interatomic distances d_{R-R} where $d_{R2-R5} < d_{R2-R1} \sim d_{R1-R1} < c < d_{R3-R4} \sim d_{R1-R3} \sim d_{R1-R4}$ are indicated

already found in the Tb-compound. The shortest interatomic $R - R$ distance is the $R1 - R3$ distance (≈3.37 Å), while the $R2 - R3$ and $R1 - R2$ distances (≈3.6 Å and ≈4.4 Å, respectively) are significantly longer and even larger than the intra sublattice $R2 - R2$ distance determined by the unit cell parameter in the c-direction. This underlines the more isolated nature of the R2 site and explains why it orders at the lowest temperature, far below the ordering temperature of the R1- and R3-sublattices. Let us recall that the R2 site remains non-magnetic in $Tb_5Ni_2In_4$ until the appearance of the additional $\kappa = (0, \delta, ½)$ contribution and that in $Ho_5Ni_2In_4$ the same site possesses, at 2 K, only a small ordered moment value within the main $\kappa = (0, 0, 0)$ order. The importance of inter-site distance dependent RKKY interactions is again reflected in the presence of an incommensurate magnetic ordering [$\kappa = (0, \delta, ½)$] which determines the ordering of the R2 sites in $Tb_5Ni_2In_4$ and probably also in $Ho_5Ni_2In_4$ at the lowest temperatures.

We would like to stress that the strong hierarchical order in which the different rare earth sites become magnetic as a function of temperature discovered here for the $R_{11}Ni_4In_9$ and $R_5Ni_2In_4$ compounds, is not primarily caused by the sole existence of different R-sublattices: e.g. $R_{15}Si_9C$ also has multiple different R-sublattices; however it has only a single magnetic propagation vector for all of the R-sublattices and all of them order at a single magnetic transition temperature [26].

For all of the four studied $R_{m+n}M_{2n}X_m$ compounds there is no indication for magnetic ordering of the Ni sites neither from the magnetic data nor from the neutron diffraction data.

4. Summary

$R_5Ni_2In_4$ and $R_{11}Ni_4In_9$ with R = Ho, Tb display a multitude of transitions as function of temperature as revealed by specific

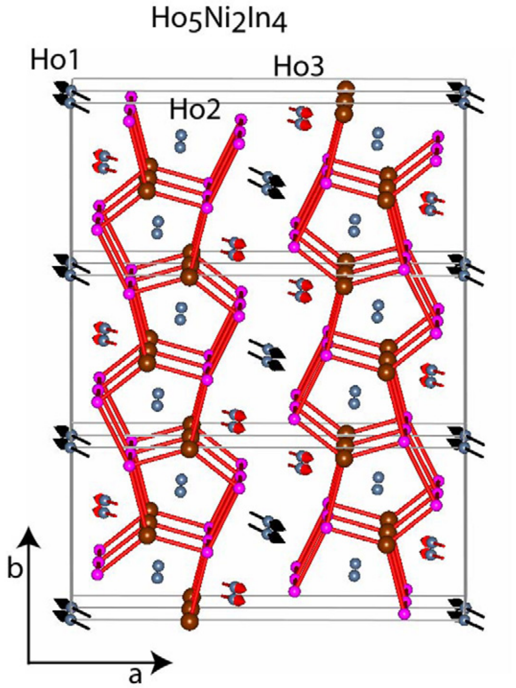

Figure 22. Magnetic order in $Ho_5Ni_2In_4$ at 25 K; Ni (brown balls), In (magenta balls). Position of the different R sites relative to the structural unit RNi_4In_6 forming rows of distorted pentagonal prisms in the b-direction; the non-magnetic Ho2 sites are situated within the RNi_4In_6 units; slightly inclined view along the c-axis.

heat, magnetic and neutron diffraction data. These transitions are of magnetic origin and are connected to the appearance of magnetic order on the different sublattices of the rare earth in the crystallographic structure. The three R-sublattices present in the $R_5Ni_2In_4$ compounds order at different temperatures in a sequence $R1(2a)$ and $R3(4g)$ together, and then $R2(4g)$ with magnetic propagation vectors $\kappa_1 = (0, 0, 0)$ and $\kappa_2 = (0, \delta, ½)$, where the second propagation vector acts mostly on the $R2$ site. A strong hierarchy among the five different R-sublattices exists for the $R_{11}Ni_4In_9$ compounds as well. As a function of decreasing temperature the magnetic ordering follows the sequence $R2(4i)$ and $R5(2a)$, then $R1(8p)$, then $R3(4i)$, then $R4(4g)$. Three or four different magnetic propagation vectors, acting within different temperature ranges and on different R-sublattices, are present in $Tb_{11}Ni_4In_9$ and $Ho_{11}Ni_4In_9$, respectively. Structural details based on the different inter- and intra-site distances are advanced to explain the sequence of the magnetic ordering processes for both $R_{m+n}Ni_{2n}In_m$ series.

Acknowledgments

The Ames Laboratory is operated by Iowa State University of Science and Technology for the U.S. Department of Energy, under Contract No. DE-AC02-07CH11358. This work was supported by the Office of Basic Energy Sciences, Materials Science and Engineering Division of the Office of Science. The samples were prepared at the Ames Laboratory, and as the magnetic and heat capacity measurements were also made at the Ames Laboratory.

References

[1] Sojka L, Manyako M, Černý R, Ivanyk M, Belan B, Gladyshevskii R and Kalychak Y 2008 *Intermetallics* **16** 625
[2] Pustovoychenko M, Tyvanchuk Y and Kalychak Y M 2010 *Intermetallics* **18** 929
[3] Provino A, Mudryk Y, Manfrinetti P, Paudyal D, Pecharsky V K and Gschneidner K A Jr 2011 *Rare Earth Research Conf.* (*Santa Fe NM, USA, 19–23 June 2011*)
[4] Provino A *et al* 2014 *Acta Mater.* **73** 27
[5] Provino A, Gschneidner K A Jr, Dhar S K, Ferdeghini C, Mudryk Y, Manfrinetti P, Paudyal D and Pecharsky V K 2015 *Acta Mater.* **91** 128
[6] Gschneidner K A Jr, Provino A, Manfrinetti P, Pecharsky V K and Mudryk Y 2013 *Proc. of the 52nd Conf. of Metallurgists, Materials Science Technology Conf. (Montréal, Québec, Canada, 27–31 October 2013)* ed I M London *et al*
[7] Szytuła A, Baran S, Przewoźnik J, Tyvanchuk Y and Kalychak Y 2014 *J. Alloys Compd.* **601** 238
[8] Szytuła A, Baran S, Penc B, Przewoźnik J, Winiarski A, Tyvanchuk Y and Kalychak Y M 2014 *J. Alloys Compd.* **589** 622
[9] Tyvanchuk Y, Baran S, Duraj R, Kalychak Y M, Przewoźnik J and Szytuła A 2014 *J. Alloys Compd.* **587** 573
[10] Zaremba V I, Kalychak Y M, Zavalii P Y and Bruskov V A 1991 *Kristallografiya* **36** 1415
[11] Provino A, Mudryk Y, Paudyal D, Smetana V, Manfrinetti P, Pecharsky V K, Gschneidner K A Jr and Corbett J D 2012 *J. Appl. Phys.* **111** 07E122
[12] Tyvanchuk Y B, Rodewald U C, Kalychak Y M and Pöttgen R 2008 *J. Solid State Chem.* **181** 878
[13] Gondek Ł, Przewoźnik J, Czub J, Tyvanchuk Y, Szytuła A and Arurlaj A 2012 *Intermetallics* **21** 10
[14] Lukachuk M, Heying B, Rodewald U Ch and Pöttgen R 2005 *Heteroatom Chem.* **16** 364
[15] Tyvanchuk Y B, Penc B, Szytuła A and Zarzycki A 2010 *Acta Phys. Pol.* A **117** 599
[16] Szytuła A, Tyvanchuk Y, Baran S, Przewoźnik J and Kalychak Y M 2013 *Intermetallics* **43** 99
[17] Materials Preparation Center, The Ames Laboratory U.S. Department of Energy, Ames, IA USA, www.mpc.ameslab.gov
[18] Rodríguez-Carvajal J 1993 *Physica* B **192** 55
[19] Pecharsky V K, Moorman J O and Gschneidner K A Jr 1997 *Rev. Sci. Instrum.* **68** 4196
[20] Gondek L, Szytula A, Baran S and Hernandez-Velasco J 2004 *J. Magn. Magn. Matter.* **272–276** e443
[21] Beaudry B J and Gschneidner K A Jr 1978 Preparation and basic properties of the rare earth metals *Handbook on the Physics and Chemistry of Rare Earths* ed K A Gschneidner Jr and L Eyring vol 1 (Amsterdam, The Netherlands: North-Holland Physics Publishing) Ch. 2 pp 173–232
[22] Tyvanchuk Y B, Kalychak Y M, Gondek L, Rams M, Szytuła A and Tomkowicz Z 2004 *J. Magn. Magn. Mater.* **277** 368
[23] Rodríguez-Carvajal J *BASIREPS*: a program for calculating irreducible representations of space groups and basis functions for axial and polar vector properties Part of the *FullProf Suite of* programs available at www.ill.eu/sites/fullprof/
[24] Ritter C 2011 *Solid State Phenom.* **170** 263
[25] Schobinger-Papamantellos P, Buschow K H J and Ritter C 1998 *J. Magn. Magn. Mater.* **186** 21
[26] Ritter C, Wrubl F, Hill A H, Pani M and Manfrinetti P 2011 *J. Phys.: Condens. Matter* **23** 296002